SCIENCE CHINA
Earth Sciences

•ARTICLE•

July 2023 Vol.66 No.7: 1622–1646
https://doi.org/10.1007/s11430-022-1047-4

Mixing processes and patterns of fluids in alkane-CO_2-water systems under high temperature and high pressure—Microscopic visual physical thermal simulations and molecular dynamics simulations

Guanghui YUAN[1,2*], Shuqi WU[1], Yingchang CAO[1,2†], Zihao JIN[1],
Keyu LIU[1] & Yanzhong WANG[1]

[1] National Key Laboratory of Deep Oil and Gas, China University of Petroleum, Qingdao 266580, China;
[2] Laboratory for Marine Mineral Resources, Qingdao National Laboratory for Marine Science and Technology, Qingdao 266071, China

Received May 16, 2022; revised December 4, 2022; accepted December 15, 2022; published online June 2, 2023

Abstract Various types of geofluids exist in deep and ultra-deep layers in petroliferous basins. The geofluids are much more active under high-temperature and high-pressure (HTHP) conditions, but their properties are unclear. We simulated the mixing of different fluids in $CH_4/C_3H_8/C_6H_{14}/C_8H_{18}$-water systems and C_6H_{14}/C_8H_{18}-CO_2-H_2O systems at temperatures of 25°C to 425°C and pressures of 5 MPa to 105 MPa, using an *in-situ* micron quartz capillary tube thermal simulation system and molecular dynamics numerical simulation software. The mixing processes, patterns, and mechanisms of various fluids were analyzed at microscale under increasing temperature and pressure conditions. The results show that the miscibility of fluids in the different alkane-H_2O and alkane-CO_2-H_2O systems is not instantaneous, but the miscibility degree between different fluid phases increases as the temperature and pressure rise during the experiments. The physical thermal experiments (PTEs) show that the mixing process can be divided into three stages: initial miscibility, segmented dynamic miscibility, and complete miscibility. The molecular dynamics numerical simulations (MDNSs) indicate that the mixing process of fluids in the alkane-H_2O and alkane-CO_2-H_2O systems can be divided into seven and eight stages, respectively. The carbon number affects the miscibility of alkanes and water, and the temperature and pressure required to reach the same miscibility stage with water increase with the carbon number (C_3H_8, C_6H_{14}, CH_4, C_8H_{18}). CO_2 has a critical bridge role in the miscibility of alkanes and water, and its presence significantly reduces the temperatures required to reach the initial, dynamic, and complete miscibility of alkanes and water. The results are of great significance for analyzing and understanding the miscibility of geofluids in deep and ultra-deep HTHP systems.

Keywords High temperature high pressure (HTHP), Alkane-H_2O-CO_2 system, Mixing of geofluids, *In-situ* visualization thermal experiments, Molecular dynamics numerical simulation

Citation: Yuan G, Wu S, Cao Y, Jin Z, Liu K, Wang Y. 2023. Mixing processes and patterns of fluids in alkane-CO_2-water systems under high temperature and high pressure—Microscopic visual physical thermal simulations and molecular dynamics simulations. Science China Earth Sciences, 66(7): 1622–1646, https://doi.org/10.1007/s11430-022-1047-4

1. Introduction

Oil and gas resources are rich in the deep to ultra-deep layers in petroliferous basins. Since these layers have not been extensively explored, they are critical for future hydrocarbon exploration (Dutton and Loucks, 2010; Jia and Pang, 2015; Ma et al., 2020; Pang et al., 2020; Li et al., 2020). Significant breakthroughs have been made in the exploration of deep and

---

* Corresponding author (email: yuan.guanghui@upc.edu.cn)
† Corresponding author (email: caoych@upc.edu.cn)

ultra-deep oil and gas layers in several large petroliferous basins, with depths greater than 4 and 6 km in East and West China, respectively (Jia and Pang, 2015; Li et al., 2020; Cao et al., 2022a). Deep and ultra-deep layers are characterized by high temperature and high pressure (HTHP). The maximum temperature of drilled ultra-deep oil and gas reservoirs exceeds 200°C in China at depths deeper than 4 km in the eastern hot basins and 6 km in the western cold basins. The fluid pressure in deep and ultra-deep layers generally exceeds 40 MPa, with maximum values exceeding 130 MPa when overpressure occurs (Pang et al., 2020; Cao et al., 2022a). The geofluids in deep to ultra-deep hydrocarbon reservoirs are more active and more complex, and their properties are unclear in HTHP conditions (Li, 2016; Yuan et al., 2019; Cao et al., 2022b). However, it is difficult to observe and detect changes in the phase states and miscibility of complex multiphase fluids in *in-situ* deep layers or under laboratory HTHP conditions. Most research on the properties and behaviors of hydrocarbon-water-CO_2 systems under HTHP conditions has been carried out using thermodynamic calculations and molecular dynamics numerical simulations (MDNSs) (Peng and Robinson, 1976; Duan et al., 2000; Duan et al., 2003; Bakker, 2012). However, few studies used direct *in-situ* observations to investigate the mixing processes and states of complex geofluids (hydrocarbon-water-CO_2 systems) under HTHP conditions in deep to ultra-deep layers (Balitsky et al., 2011a, 2011b).

In-situ micro thermal experiments typically use quartz capillary tubes and diamond pressure chambers to conduct physical thermal experiments (PTEs) to study HTHP fluids. HTHP optical quartz cells (HTHPOCs) have the advantages of easy preparation, low sample size, strong thermal conductivity, high light transmission efficiency, and resistance to HTHP and corrosion (Chou et al., 2008; Wang et al., 2011, 2017; Ni et al., 2011; Wan et al., 2021). Many achievements have been made using microscopic experiments to analyze the phase changes of single component fluids and relatively simple composite fluids ranging from low-temperature-low pressure (LTLP) to HTHP conditions. In addition, the miscibility processes of oil-CO_2-water systems have been evaluated under relatively low-temperature conditions (Yang et al., 2005; Chou et al., 2008; Ni et al., 2011; Guo et al., 2014; Ou et al., 2015; Li et al., 2016; Pruteanu et al., 2017). However, more research is required on complex hydrocarbon-water-CO_2 systems under geological HTHP conditions. Although microscopic *in-situ* experiments on geofluids have been conducted, they have typically focused on characterizing phenomena or explaining microscopic phenomena using existing theories. MDNSs combine theories and physical experiments to understand micro- and macro-scale phenomena. They can provide a molecular-atomic-level understanding of fluid evolution and relevant mechanisms (Duan et al., 2000; Lu and Berkowitz, 2004; Headen and Boek, 2011; de Lara et al., 2012). Researchers have conducted many MDNSs of typical geofluid systems in hydrocarbon reservoirs containing hydrocarbons, water, and CO_2. However, these studies have primarily focused on the physical and chemical properties of fluids in a wide temperature and pressure (*T-P*) range (Zhang and Duan, 2005; Zhang et al., 2013; Zhang et al., 2015), or on the interface characteristics and their changes over time at relatively LTLP conditions (Carpenter and Hehre, 1990; da Rocha et al., 2001; Kunieda et al., 2010; Zhao et al., 2011; Li et al., 2013). To date, few studies have been conducted on miscibility processes and their mechanism of geological HTHP hydrocarbon water (-CO_2) systems in deep to ultra-deep layers. In addition, MDNSs have not been combined with microscale PTEs.

In this paper, a series of MDNSs and *in-situ* visualization PTEs within HTHPOCs are conducted using representative fluids common in deep and ultra-deep hydrocarbon reservoirs (CH_4, C_3H_8, C_6H_{14}, C_8H_{18}, H_2O, and CO_2). The miscibility and mechanisms of the different fluids in various $CH_4/C_3H_8/C_6H_{14}/C_8H_{18}$-water systems and C_6H_{14}/C_8H_{18}-CO_2 water systems are analyzed from LTLP to HTHP conditions. The results can provide scientific information for designing HTHP thermal experiments, analyzing the mechanisms of geofluid-rock interactions, and guiding the exploration and development of deep and ultra-deep HTHP hydrocarbon reservoirs.

2. Samples and methods

2.1 Microscopic visual physical thermal experiments

2.1.1 Samples and equipments

The components of geofluids in deep and ultra-deep hydrocarbon reservoirs are complex. Hydrocarbons are primarily natural gas and condensates, and liquid hydrocarbons are also present (Zhu et al., 2019; Pang et al., 2020; Zhu et al., 2021; Peng and Jia, 2021). In addition to hydrocarbons, CO_2, a natural gas component, is common in hydrocarbon reservoirs. The content of CO_2 is generally lower than 5%. As the increase of burial depth and temperature increase, the CO_2 content in deep to ultra-deep hydrocarbon reservoirs can reach 5–10% (Smith and Ehrenberg, 1989; Seewald, 2003; Cao et al., 2022b). If there are deep CO_2 sources, a large amount of CO_2 can accumulate together with hydrocarbons to form reservoirs (Liu et al., 2017, 2019; Chen et al., 2017). Pore water also exists in most hydrocarbon reservoirs (Zhao et al., 2018; Yuan et al., 2019; Cao et al., 2022b). This study uses high-purity hydrocarbons, including gaseous methane (99.999%) and propane (99.9%), as well as low molecular weight liquid hydrocarbons (n-hexane (>99.5%) and n-octane (>99.5%)) as representative alkanes to analyze the mixing processes of different fluids in the thermal experiments. Ultra-pure water and high-purity CO_2 (>99.8%) are selected for the miscibility experiments.

The microscopic visualization PTEs on several alkane-water systems and alkane-CO_2-water systems were conducted using an *in-situ* microcapillary thermal experiment system (Figure 1) at temperatures of 25°C to 425°C and pressures of 5 to 105 MPa. This device can be used for real-time visual observations, *in-situ* detection, and analysis of the mixing process of geofluids under HTHP. This system is an improved version of existing experimental equipment (Chou et al., 2008; Wang et al., 2011, 2017, 2020; Xu and Chou, 2017). It consists of the HTHP quartz capillary tube thermal system (Chou et al., 2008; Wang et al., 2011), microscope, high-resolution laser confocal micro Raman spectrometer (LabRam HR Evolution), video recording software, vacuum pump, and gas cylinder. The quartz capillary tube thermal system is composed of a quartz capillary tube optical reaction cell (HTHPOC), a constant pressure liquid pump, and a heating-cooling stage (LinkamCAP-500, −196–500°C). Studies have shown that the temperature difference within 4 cm in the middle of this type of heating-cooling stage is less than 0.5°C, and the temperature distribution is uniform (Wang et al., 2017). The pressure sensor (0–1500 bar) is located between the HiP high-pressure needle valve (30–15HF430000 psi) and the HTHPOC to measure the fluid pressure inside the capillary tubes. In addition, a manual precise tuning wheel (screw rod model 1204) is employed to fix the high-pressure needle valve with the HTHPOC, which can adjust the observation field of the HTHPOCs in the limited observation range of the window of the heating-cooling stage during the experiments to facilitate the *in-situ* laser Raman measurements.

2.1.2 *Sample preparation and experiment process*

We used a ceramic knife to cut the coarse quartz capillary tubes (TPS200794, with an inner diameter of 200 μm and outer diameter of 794 μm). A hydrogen-oxygen torch was used for welding both ends of the capillary tubes, burning off the brown protective coating on one end, and exposing a transparent section of about 4 cm for *in-situ* observation and online detection. We inserted the other end of the coarse capillary tube into the sealing component composed of a 3 cm high-pressure stainless-steel tube and its supporting conical sleeve. The end of the capillary extended about 2 mm beyond the end of the conical sleeve and was sealed with AB glue. We cut off the end of the capillary and left about 1 mm for subsequent sample adding. The HTHPOCs were ready for the thermal experiments. Then we cut a fine quartz capillary tube (TPS075150, inner diameter 75 μm, outer diameter 150 μm). One end was inserted into a disposable syringe needle and beyond the needle, plug to prevent the fine capillary tube from becoming stuck. We then sealed the tube and the needle with AB glue, and the other end was left untreated to add the liquid sample to the coarse HTHPOC. We created several groups to add the samples to ensure that the sample was not polluted and wiped the fine tubes with alcohol before adding the samples. To inject gases into the HTHPOC, we intercepted a fine quartz capillary tube. One end of the tube received the same treatment as the open end of the coarse HTHPOC, and was then connected to the gas cylinder through screws, connectors, and high-pressure valves.

We used different processes to add different samples to the HTHPOC: (1) CH_4/C_3H_8 and water. We drew a certain amount of water into a syringe connected to a fine tube and inserted the fine tube with the water into the end of the HTHPOC with the closed bottom. We slowly pulled the fine tube out while pressing the spying handle until the HTHOPC was filled with water. We opened the valve of the gas cylinder and used the gas to flush the line. We inserted the fine tube connected to the cylinder into a vessel with water. The bubbling speed was controlled to about one bubble per second to prevent the complete discharge of water from the HTHPOC. We inserted the fine tube into the HTHPOC at approximately 5 mm from the bottom and slowly removed the fine tube to discharge the water into the coarse tube (about 5 mm was left at the bottom). After the fine tube was removed, the HTHPOC was connected to the high-pressure needle valve on the sliding table and vacuumized. To have sufficient gas in the HTHPOC, the CH_4 or C_3H_8 in the gas cylinder was injected into the HTHPOC at a pressure reaching 0.4 MPa. Finally, the constant-pressure liquid pump was used to add water to the HTHPOC to reach a pressure of 20 MPa (close to the critical pressure of alkanes at room temperature). The length of the water and CH_4/C_3H_8 in the HTHPOC was approximate 5 mm each, and the remainder of the tube was filled with water (Figure 2a1, 2a2). (2) C_6H_{14}/C_8H_{18} and water. We used the same steps as above to fill the coarse HTHPOC with water and the same process to inject the liquid alkanes into the bottom of the HTHPOC with a fine tube. When the fine tube was about 5 mm from the bottom, it was quickly removed from the HTHPOC. We connected the HTHPOC to the high-pressure needle valve on the sliding table and used liquid nitrogen to freeze the liquid alkane at the closed end of the HTHPOC. The tube was vacuumized and the constant-pressure liquid pump was used to add water to reach a pressure of 20 MPa. The length of C_6H_{14}/C_8H_{18} at the bottom of the HTHPOC was approximate 5 mm, and the remainder of the tube was filled with water (Figure 2a3, 2a4). (3) C_6H_{14}/C_8H_{18}, water and CO_2. We filled the coarse HTHPOC with water in the same way and inserted the fine tube containing liquid alkane into the HTHPOC at about 2 mm from the closed bottom. We push the spring handle and slowly removed the fine tube. When the fine capillary tube was about 4 mm from the closed end, it was quickly pulled out. We add CO_2 into HTHPOC using the same steps for

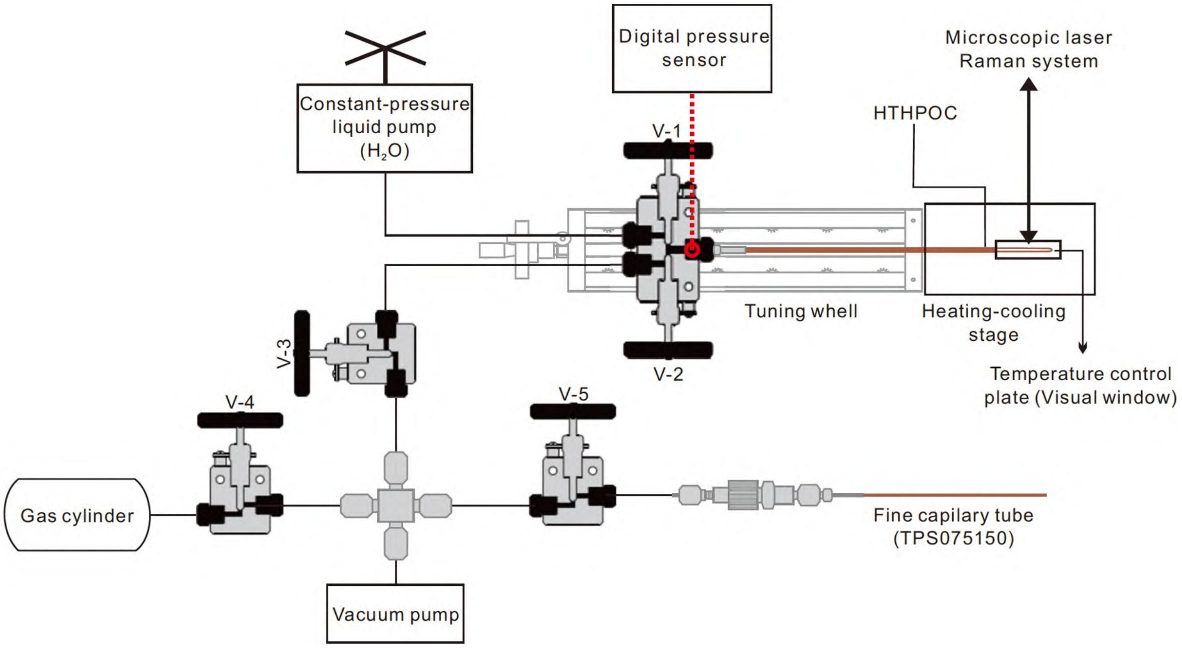

Figure 1 Schematic diagram of the thermal experiment and the optical quartz capillary tube system.

CH_4/C_3H_8 and water and pressurized it to 0.4 MPa. Finally, we used the constant-pressure liquid pump to add water to the HTHPOC to reach a pressure of 5 MPa (lower than the critical pressure of CO_2). The HTHOPC contained approximately 2 mm of H_2O, 2 mm of C_6H_{14}/C_8H_{18}, and 10 cm of CO_2. The remainder of the tube was filled with water (Figure 2b1, 2b2). The initial states of the CH_4/C_3H_8/C_6H_{14}/C_8H_{18}-water and C_6H_{14}/C_8H_{18}-CO_2-water systems in the HTHPOC are shown in Figure 2. The mixed fluids are located within 1–1.5 cm of the bottom of the capillary tubes. During the experiments, they are located in the middle of the heating-cooling stage to ensure a uniform temperature of the fluid systems.

We insert the closed end of the HTHPOC into the heating-cooling stage and placed the transparent section of the HTHPOC above the temperature control plate. The HTHPOC was covered with a thin, hollow silver cover to prevent it from shaking or warping and facilitate the focusing of the microscope and laser. The *T-P* of the experimental systems were controlled by the heating-cooling stage and the-constant pressure liquid pump, respectively. The *T-P* combination was adjusted according to the geothermal gradient of 4–4.5°C/100 m in hot basins to simulate deep/ultra-deep geological conditions. When the temperature was lower than 150°C in the experiments, it was kept constant for 10–20 min after reaching each *T-P* condition. When the temperature exceeded 150°C, it was kept constant for 2–4 h after reaching each critical *T-P* condition to reach a stable state of the fluid system. During the thermal experiments, the micro-Raman spectrometer was used to excite 532 nm green light for *in-situ* detection to obtain the Raman spectrogram. Qualitative analysis of the fluids was conducted at the interface and its vicinity. The oCam video recording software was used to record the miscibility states of the systems in real-time.

2.2 Molecular dynamics simulations

2.2.1 Model construction

The MDNSs were carried out using the Materials Studio (MS) software package developed by Accelrys. The COMPASS force field (Sun et al., 1998; Yang et al., 2010; Wang et al., 2005; Zhong et al., 2013), which is applicable to organic and inorganic molecular systems, was used to determine the force field parameters of the alkanes, water, and CO_2 in the simulations.

The molecular models of individual components were established, and their geometric configurations were optimized. Simulation boxes with molecules of single components were constructed. The four types of alkanes analyzed in the MDNSs are methane, propane, n-hexane, and n-octane, the same as the visualization PTEs. The number of molecules, initial density, and the box size of the single-component systems of the alkanes, water, and carbon dioxide are listed in Table 1. The initial density was obtained from the experimental data of the American Standard Library (NIST). The *c* value of the box size in the *z*-direction is determined by *a*, *b*, the number of molecules, and the initial density of the system. Simulation boxes with multiple components of the four types of alkane-water and two types of alkane-CO_2-water systems were constructed by copying and translation. The box size increased with the value of *a*

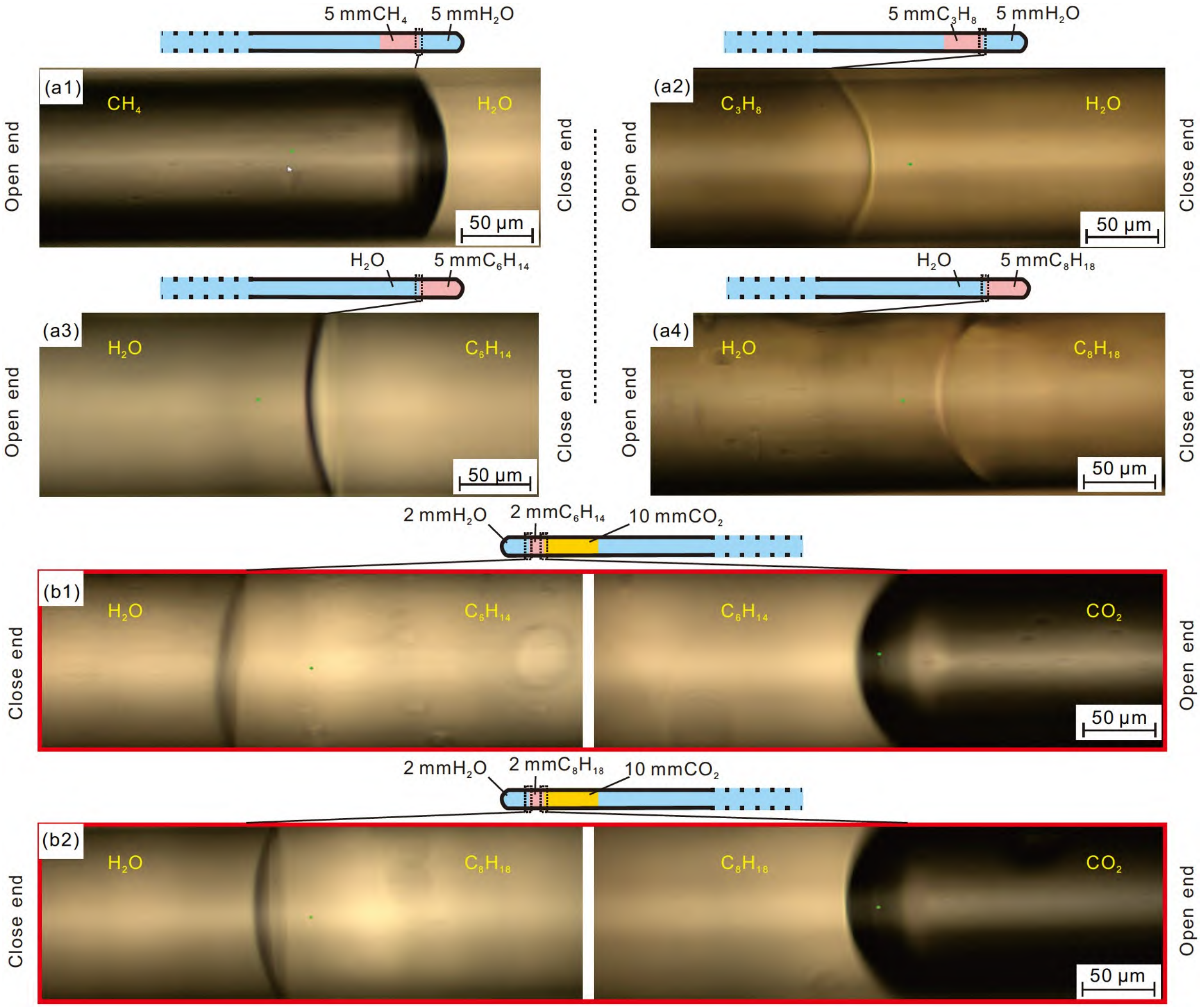

Figure 2 Fluid distribution and the initial state of each system in capillary thermal experiments. (a1)–(a4) Alkane-water systems at initial 25°C/20 MPa; (b1)–(b2) Alkane-CO_2-water system at initial 25°C/5 MPa.

Table 1 Molecular model composition of single-component systems[a)]

Molecule	No. of molecules	Initial density (g cm^{-3})	Box size of single-component system (Å)		
			a (*x*)	*b* (*y*)	*c* (*z*)
CH_4	220	0.000648	30	30	9082.297
C_3H_8	200	0.00181	30	30	8990.150
C_6H_{14}	150	0.655	30	30	35.919
C_8H_{18}	120	0.698	30	30	35.824
H_2O	1200	0.997	30	30	39.886
CO_2	600	0.00178	30	30	24.396

a) T=25°C, P=0.1 MPa

only in the *x*-direction. Note that the size of a single molecule in the box did not increase with the box size. The values were based on the standard to ensure that the systems in the box did not contact each other.

2.2.2 Simulation details and analysis methods

After the initial construction of the multi-component simulation box, geometry optimization of the multi-component system was performed using the Geometry Optimization tool in the Force module. An initial structural model of each multi-component system was constructed using the preliminary dynamics simulation calculation of the module. The truncation radius was 1 nm, the simulation time step was 1 fs, and one frame was output every 2000 ps as the system track file. The simulation system used three-dimensional periodic boundary conditions to eliminate the influence of boundary effects and obtain a more realistic simulation environment (Yan and Zhu, 2013). We simulated 20 ps using the isothermal isobaric ensemble (NPT) to ensure that the alkane-water and alkane-CO_2-water systems reached an initial *T-P* of 25°C/20 MPa and 25°C/5 MPa, respectively, to establish the initial models of the multi-component systems. We derived the relative concentrations of single-component and multi-component of the initial configurations (Figure 3). The models of the water-alkane-water systems were symmetrical, and those of the water-CO_2-alkane-water systems were semi-symmetrical to prevent the movement of molecules between the boxes and the adjacent mirror boxes at the interface due to periodic boundary conditions and the distortion of the molecular miscibility state of the system.

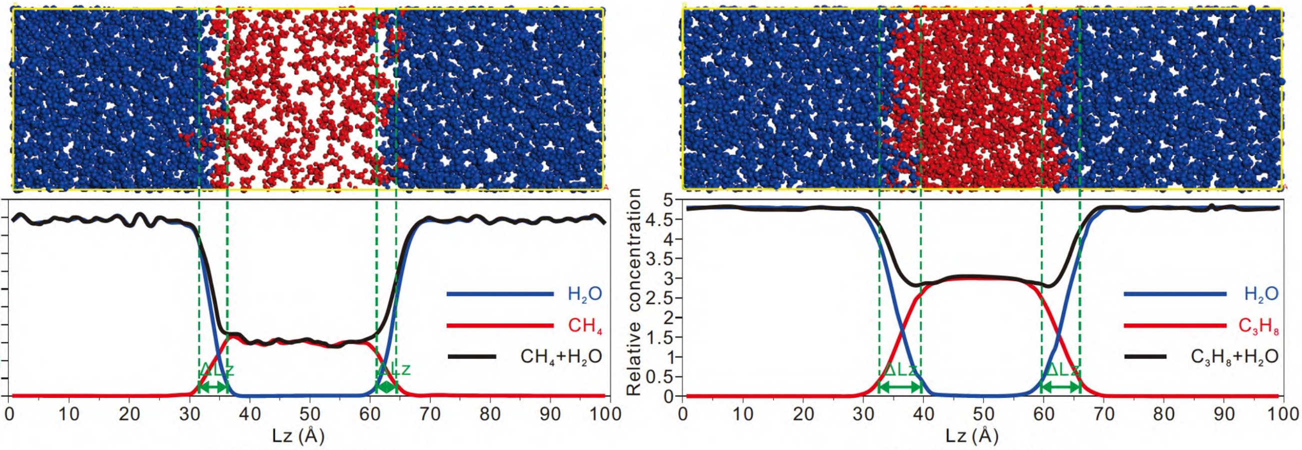

(a) CH_4-H_2O system (b) C_3H_8-H_2O system

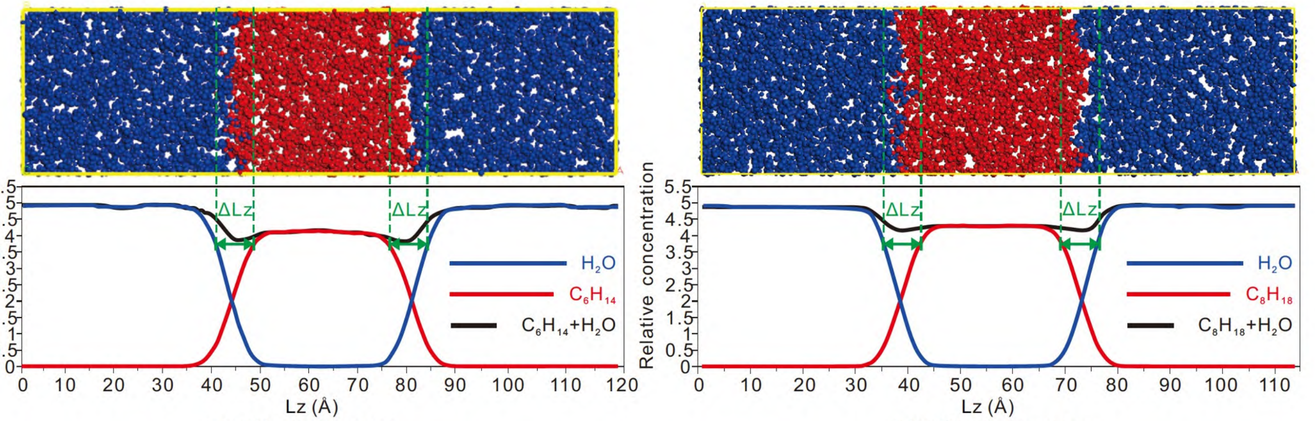

(c) C_6H_{14}-H_2O system (d) C_8H_{18}-H_2O system

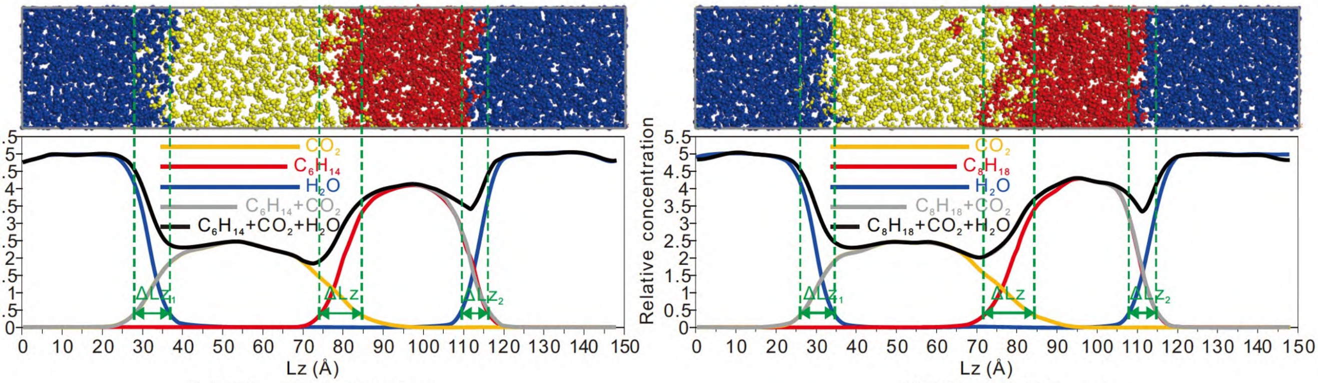

(e) C_6H_{14}-CO_2-H_2O system (f) C_8H_{18}-CO_2-H_2O system

ΔLz -alkane | water or alkane | CO_2 ΔLz$_1$ -water | CO_2 ΔLz$_2$ -alkane | water

Figure 3 Initial configuration diagrams and relative concentration distributions of fluids in each system. (a)–(d) alkane-water systems at 25°C/20 MPa, NPT20ps; (e)–(f) alkane-CO_2-water systems at 25°C/5 MPa, NPT20ps.

Based on the initial structure models, additional 200–800 ps MDNSs were conducted using the NVT ensemble (constant atomic number, temperature, and volume) under the initial *T-P* conditions. The transient trajectory of the system was saved every 20000 steps (20 ps) to record the system's evolution. Following this simulation method, i.e., initial 20 ps simulations using the NPT ensemble and additional 200–800 ps simulations using the NVT ensemble (NPT20ps-NVT200–800ps), MDNSs were carried out for every *T-P* condition corresponding to the visual PTEs. The instantaneous configurations of the fluids' mixing states in the alkane-water systems and alkane-CO_2-water systems were obtained at the last moment of each step under different *T-P* conditions. The relative concentrations of single-component and multiple-components for each instantaneous configuration were obtained. According to the "10–90" principle (Yuet and Blankschtein, 2010; Zhao et al., 2011), the width of the interface in the alkane-water system was the distance between the positions corresponding to 10% water concentration and 10% alkane concentration in the *x*-direction. The width of the interface in the alkane-CO_2-water systems was the distance between the positions corresponding to 10% water concentration and 10% alkene (CO_2 or alkane+CO_2) concentration in the *x*-direction. The interface widths of the systems under different *T-P* conditions are listed in Table 2.

3. Results

3.1 CH_4-H_2O system

A clear interface exists between the CH_4 phase and water phase in the CH_4-water system in the PTE at 25°C/20 MPa (Figure 2a1). However, a significant CH_4 Raman signal is detected in the water phase (Figure 4b1). Water droplets are observed in the CH_4 at 50°C/20 MPa. As the temperature increases, more water droplets appear and some coalesce to become larger (Figure 4a1). At 170°C/20 MPa, very small oil droplets appear in the water phase near the interface (Figure 4a2, 4b1). At 220°C/40 MPa, the water droplets in the CH_4 zone aggregate, forming water-rich segments. As the *T-P* increases, the water-rich segments and alkane-rich segments mix and separate repeatedly, and the volume and length of the segments decrease (Figure 4a3–4a5). At 360°C/90 MPa, an extensive exchange of CH_4 and water occurs at the interface (Figure 4a6). Eventually, the CH_4 and

Table 2 Widths of Interfaces in different systems under different *T-P* conditions[a)]

CH_4-H_2O		C_3H_8-H_2O		C_6H_{14}-H_2O		C_8H_{18}-H_2O	
T/*P*	$\overline{\Delta Lz}$ (Å)	*T*/*P*	$\overline{\Delta Lz}$ (Å)	*T*/*P*	$\overline{\Delta Lz}$ (Å)	*T*/*P*	$\overline{\Delta Lz}$ (Å)
25°C/20 MPa	3.75	25°C/20 MPa	6.5	25°C/20 MPa	7.25	25°C/20 MPa	7.75
50°C/20 MPa	4	100°C/20 MPa	7	150°C/20 MPa	8	150°C/20 MPa	8.5
170°C/20 MPa	7	200°C/30 MPa	8.5	210°C/40 MPa	8.5	260°C/70 MPa	9.5
220°C/40 MPa	12.75	275°C/80 MPa	12.75	250°C/60 MPa	9.5	300°C/80 MPa	10.5
360°C/90 MPa	75	300°C/80 MPa	16.25	320°C/80 MPa	12	375°C/95 MPa	13.5
408°C/100 MPa	∞100	350°C/85 MPa	75	375°C/95 MPa	17.75	400°C/100 MPa	17.75
		360°C/90 MPa	∞100	404°C/100 MPa	36	423°C/105 MPa	19.5
				450°C/110 MPa	∞120	450°C/110 MPa	30
						500°C/115 MPa	∞130

C_6H_{14}-CO_2-H_2O				C_8H_{18}-CO_2-H_2O			
T/*P*	ΔLz_1 (Å)	ΔLz_2 (Å)	$\overline{\Delta Lz}$ (Å)	*T*/*P*	ΔLz_1 (Å)	ΔLz_2 (Å)	$\overline{\Delta Lz}$ (Å)
25°C/5 MPa	8.8	6.4	7.3	25°C/5 MPa	8.4	6.2	7.3
25°C/8 MPa	11.5	8	9.75	25°C/8 MPa	11.2	7.4	9.3
25°C/20 MPa	11.2	7.8	9.5	25°C/20 MPa	11	7.4	9.2
150°C/20 MPa	22.2	13.2	17.7	150°C/20 MPa	23.2	10.4	16.8
210°C/40 MPa	31.6	18.8	25.2	260°C/70 MPa	39.3	31.2	35.25
250°C/60 MPa	47.3	23.3	35.3	300°C/80 MPa	46.8	43.2	45
320°C/80 MPa	50.5	44	47.25	375°C/95 MPa		∞155	
375°C/95 MPa		∞158		400°C/100 MPa		∞155	
404°C/100 MPa		∞160		423°C/105 MPa		∞158	
430°C/105 MPa		∞160		450°C/110 MPa		∞160	

a) $\overline{\Delta Lz}$ is the average interface width, ΔLz_1 is the interface width between the water on the left side and CO_2 or alkane+CO_2, and ΔLz_2 is the interface width between the water on the right side and alkane or alkane+CO_2.

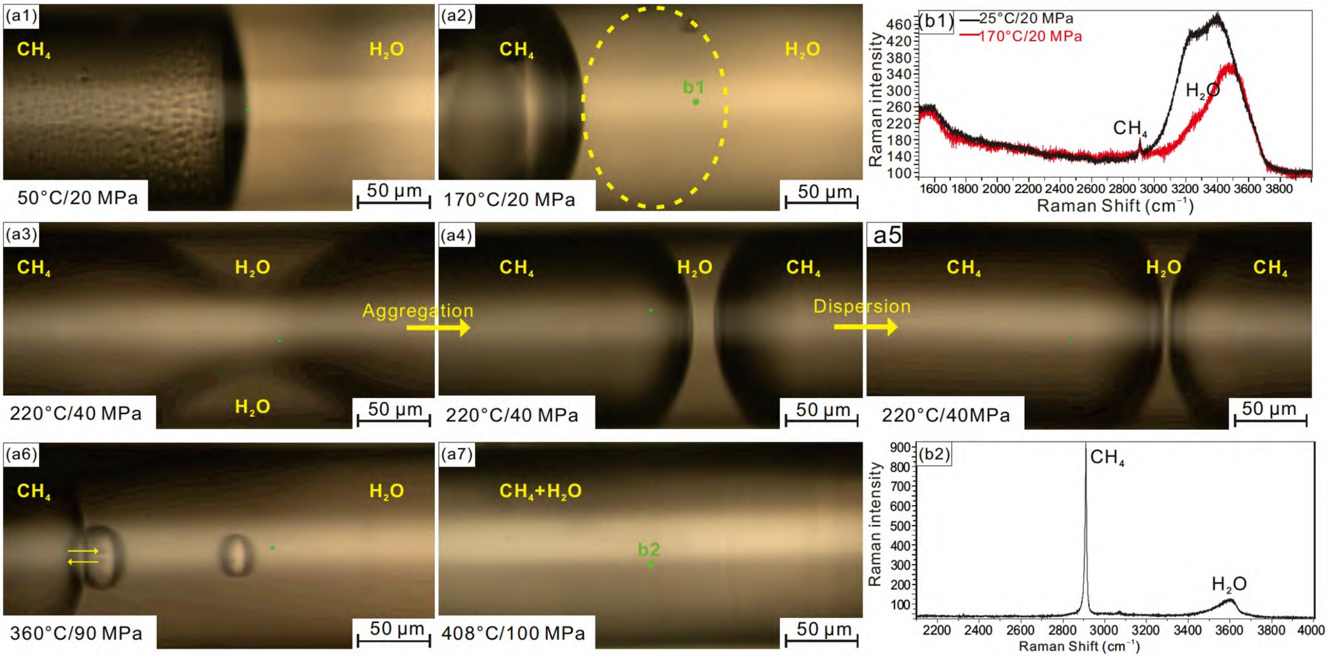

Figure 4 Miscibility features of fluids in the CH_4-H_2O system in HTHPOC and *in-situ* Raman spectrum.

water become completely miscible at 408°C/100 MPa (Figure 4a7), and significant Raman signals of CH_4 and water are detected in the miscible solution (Figure 4b2).

In the MDNS, the CH_4-water system at 50°C/20 MPa can be divided into three parts: a pure zone, interface zone, and pure CH_4 zone. A clear interface exists between the water and CH_4 phases, and only a few water and CH_4 molecules appear, respectively, in the CH_4 phase and water phase near the interface (Figure 5a). At 170°C, the interface remains stable, but there are more water molecules in the CH_4 zone and more CH_4 molecules in the water zone (Figure 5b). At 220°C/40 MPa, more water molecules appear in the CH_4 zone and CH_4 molecules in the water zone, and the same molecules tend to aggregate, consistent with the segmented dynamic miscibility in the PTEs under the same *T-P* condition. In addition, the interface between CH_4 and water is indistinct (Figure 5c). At 360°C/90 MPa, the interface in the instantaneous configuration of the CH_4-water system has almost disappeared (Figure 5d), but the relative concentration curves still indicate the existence of an ambiguous interface (Figure 5f). In combination with the active oil-water exchange near the interface in the PTEs under the same *T-P* conditions, this discrepancy is probably caused by the small spatial scale of the MDNS, which can only reflect local phenomena near the interface. At 408°C/100 MPa, the interface has disappeared completely, and the two types of molecules are mixed. The CH_4 and water molecules are uniformly distributed in the system (Figure 5e), and the relative concentration curves of the individual components show no fluctuations (Figure 5e).

3.2 C_3H_8-H_2O system

In the PTE, C_3H_8 changes into liquid at 25°C and 20 MPa, and a clear interface exist between the liquid C_3H_8 and water phases (Figure 2a2). At 100°C/20 MPa, the C_3H_8 and water are partially miscible, and more water droplets occur in the C_3H_8 zone than oil droplets in the water zone (Figure 6a1). At 200°C/30 MPa, the oil droplets in the water become larger and are distributed dispersedly (Figure 6a2), and the water droplets in the C_3H_8 zone coalesce to form water sheets (Figure 6a3). Laser Raman analysis at the position of the oil droplets showed significant Raman peaks of C_3H_8 and water (Figure 6b). At 275°C/80 MPa, the two fluids become miscible instantaneously and then separate and mix dynamically (Figure 6a5), eventually becoming completely miscible.

In the MDNSs, the C_3H_8-water system at 100°C/20 MPa can be divided into three parts: a water zone, an interface zone, and C_3H_8 zone. A clear interface exists between the water and C_3H_8 phases, while some water and C_3H_8 molecules are mixed near the interface (Appendix Figure S1a, https://link.springer.com). At 200°C/30 MPa, more water molecules occur in the C_3H_8 zone, and more C_3H_8 molecules pass the interface and dissolve into the water (Figure S1b). At 275°C/80 MPa, the number of water molecules in the C_3H_8 zone and the number of C_3H_8 molecules in the water zone have increased significantly, and the same molecules show an aggregation trend; however, the interface remains (Figure S1c). At 275°C/80 MPa, the mixing state of the system in the MDNS differs from the instantaneous complete miscibility of the two different phases in the PTE. The in-

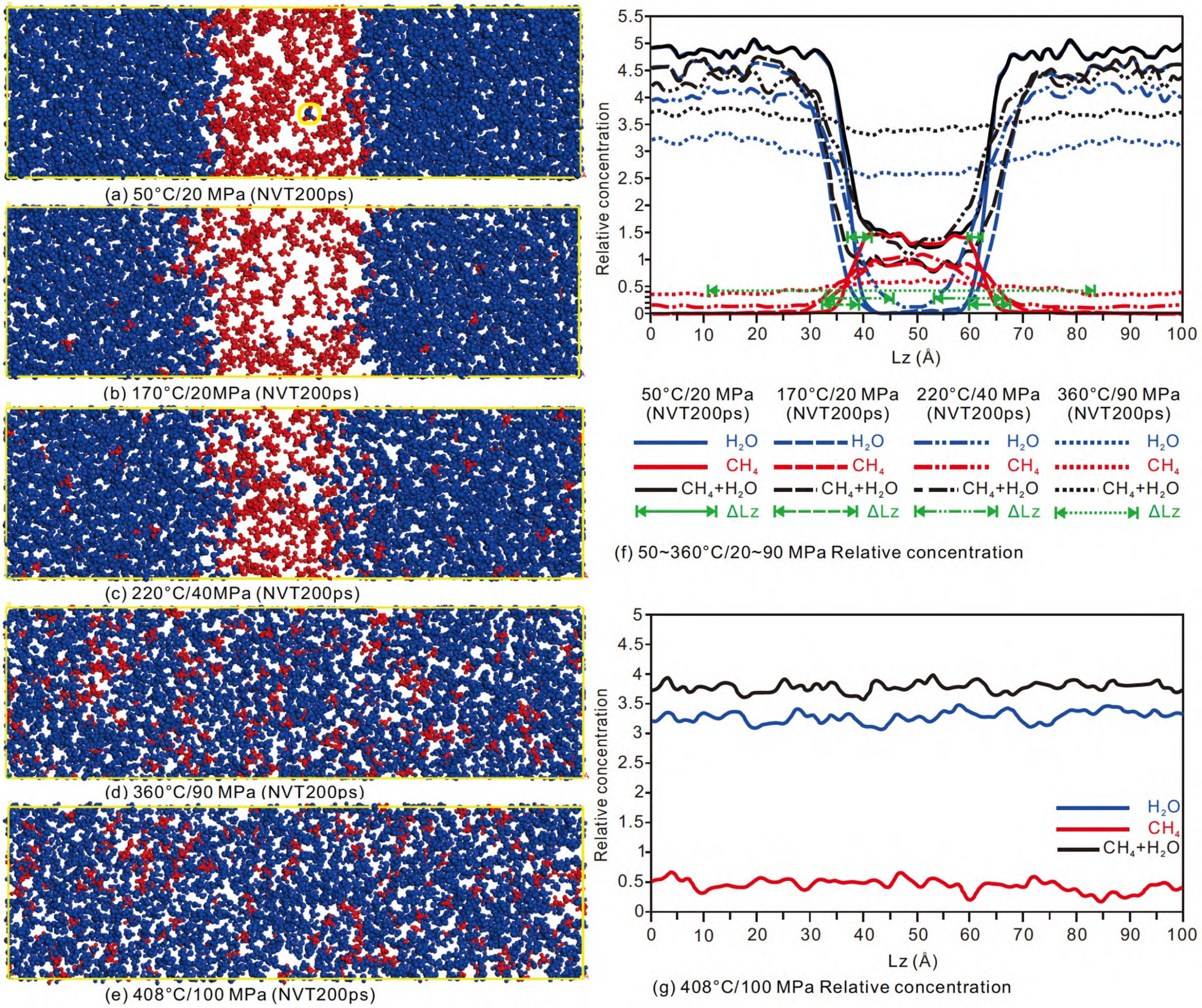

Figure 5 Instantaneous configurations and relative concentration curves of the CH_4-H_2O systems in the MDNSs.

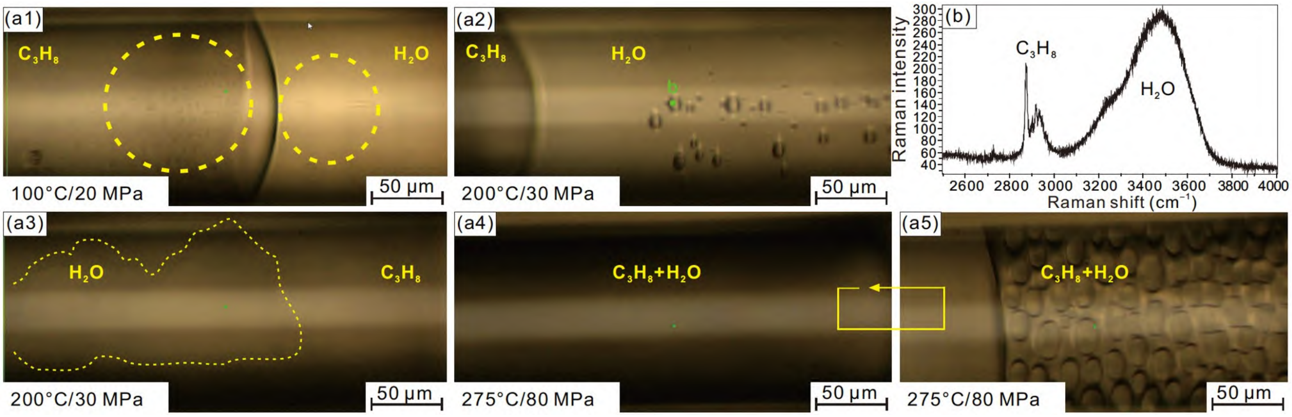

Figure 6 Miscibility features of fluids in the C_3H_8-H_2O system in the HTHPOC and *in-situ* Raman spectrum.

terface becomes less clear at 800 ps of the simulation. At this time, more water molecules rush into the C_3H_8 area and aggregate, and more C_3H_8 molecules exist in the water zone (Figure S1d). The relative concentration curves also reflect the existence of the interface (Figure 1h). This reason for the difference may be that the MDNSs duration is much shorter than PTEs duration. The subsequent continuous numerical simulations at higher *T-P* show that the degree of overlap between the C_3H_8 and water molecules is higher (Figure S1e, S1f). Finally, the instantaneous configuration and the relative concentration show that the C_3H_8-water system has reached a completely miscible state at 360°C/95 MPa in the MDNSs (Figure S1g, S1i).

3.3 C_6H_{14}-H_2O system

In the C_6H_{14}-water system, a few oil droplets are identified in the water phase from 25°C/20 MPa (Figure 2a3) to 150°C/20 MPa (Figure 7a1). At 200°C/30 MPa, an oil droplet is observed in the water phase near the oil-water interface (Figure 7a2). The Raman spectrum on the oil droplet position shows signals of n-hexane and water (Figure 7b1), and the intensity is much stronger for the water than that for n-hexane. At 210°C/40 MPa, water nodules appear in the oil phase (Figure 7a3). *In-situ* laser Raman spectroscopy shows a peak at approximately 3630.68 cm^{-1} (Figure 7b2). It is attributed to the stretching vibration of water molecules in the range of 3000–3800 cm^{-1} (Pironon et al., 2003; Chen et al., 2007) but is different from the typical Raman spectral response of water. It is similar to the Raman peak generated by H_2O or OH in a heated quartz tube found by Xu and Chou (2017) in a high-temperature experiment. This similarity indicates that water is mixed with the oil phase under these *T-P* conditions, but the amount of water is small, and water molecules have penetrated into the quartz capillary tube due to the HTHP. At 250°C/60 MPa, the oil droplets in the water phase have coalesced and are larger (Figure 7a4). At 320°C/80 MPa, the water begins to converge in the oil phase (Figure 7a5). At 375°C/95 MPa, the system exhibits local miscibility at the oil-water interface, accompanied by an enlargement of the oil droplets in the water phase (Figure 7a6). At 380°C/95 MPa, extensive mass exchange occurs across the interface, and more oil droplets appear in the water phase within a certain range near the interface. The oil droplets become larger due to rapid aggregation and dispersion (Figure 7a7). At 402°C/100 MPa, the interface is indistinct and shifts quickly in the tube (Figure 7a8). Finally, at 404°C/100 MPa, the interface has completely disappeared (Figure 7a9), indicating complete miscibility of the C_6H_{14} and water phases. Although the HTHP caused a substantial drift in the Raman spectral baseline, significant Raman peaks of C_6H_{14} and water are detected in the mixed liquid after complete miscibility (Figure 7b3).

At 150°C/20 Ma in the MDNS, the C_6H_{14}-water system can still be divided into three parts, including a water zone, interface zone, and C_6H_{14} zone. A clear interface exists between the water and C_6H_{14} phases. Slight miscibility of water and C_6H_{14} is observed at the interface area. In addition, the C_6H_{14} molecules pass through the interface and enter into the water zone (Figure 8a), indicating that although the two phases are immiscible under this condition, some C_6H_{14} molecules have dissolved in the water. At 210°C/40 MPa, the

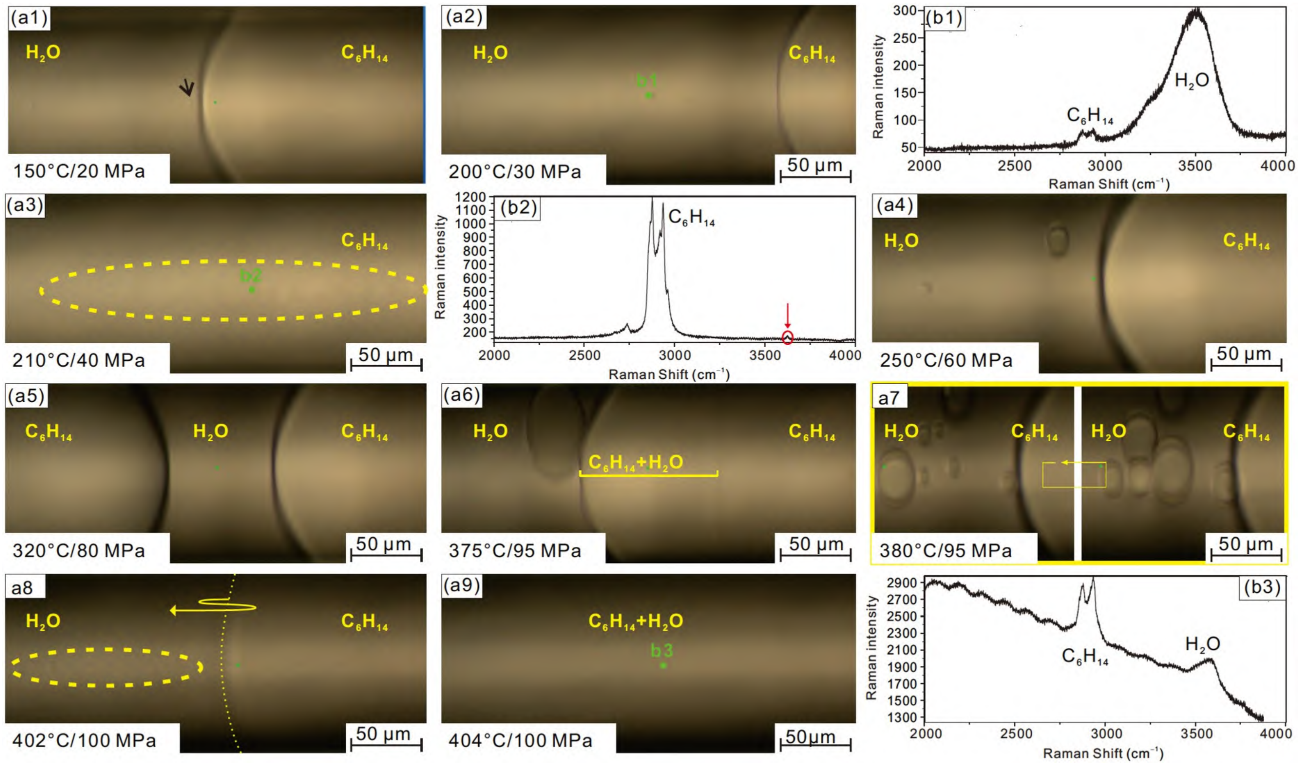

Figure 7 Miscibility features of C_6H_{14}-H_2O system in the HTHPOC and *in-situ* Raman spectra.

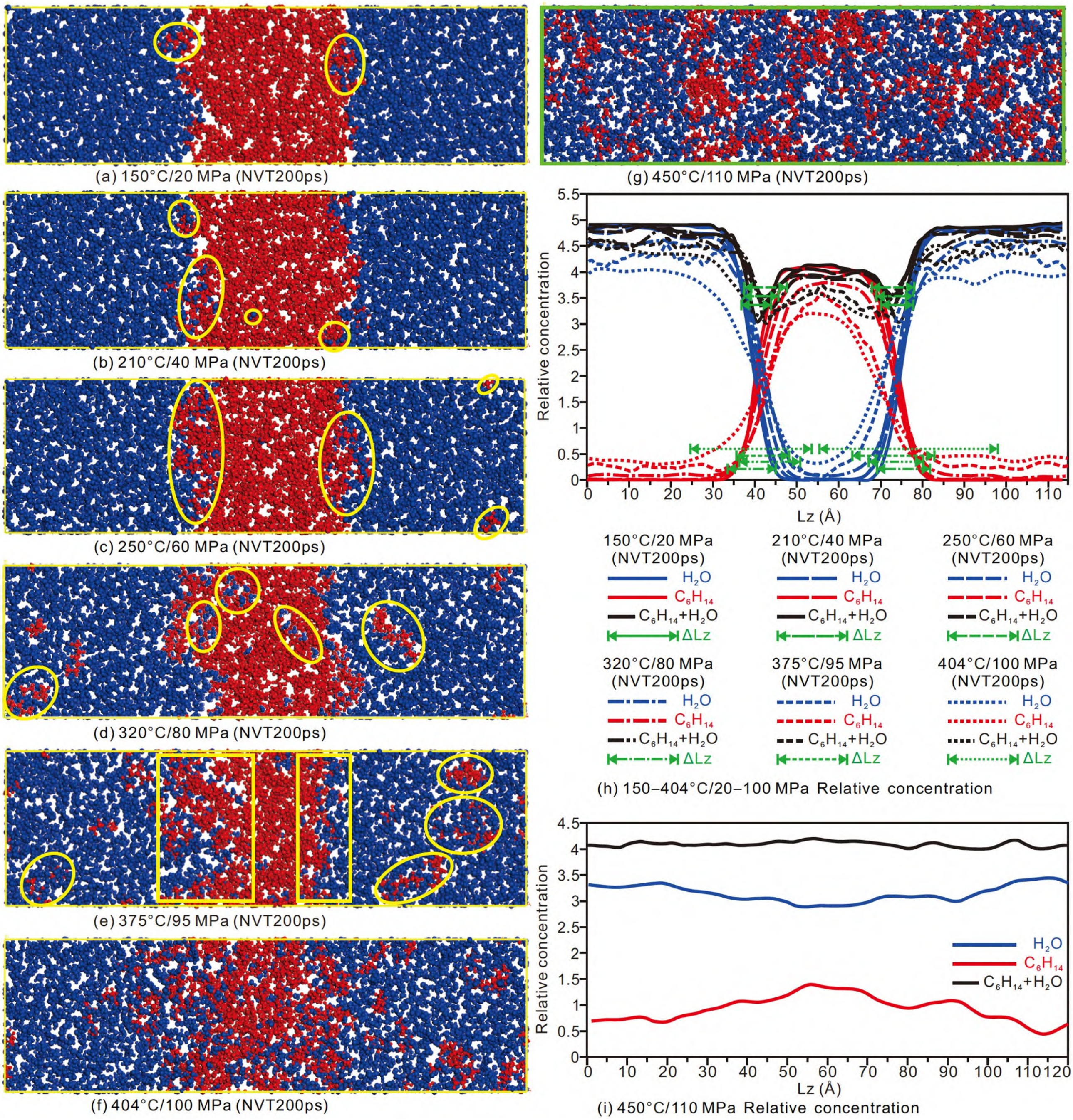

(a) 150°C/20 MPa (NVT200ps)

(b) 210°C/40 MPa (NVT200ps)

(c) 250°C/60 MPa (NVT200ps)

(d) 320°C/80 MPa (NVT200ps)

(e) 375°C/95 MPa (NVT200ps)

(f) 404°C/100 MPa (NVT200ps)

(g) 450°C/110 MPa (NVT200ps)

(h) 150–404°C/20–100 MPa Relative concentration

(i) 450°C/110 MPa Relative concentration

Figure 8 Instantaneous configurations and relative concentration curves of the C_6H_{14}-H_2O systems in the MDNSs.

number of water molecules in the local C_6H_{14} phase has increased significantly near the interface, and a water molecule has entered the inner part of the C_6H_{14} phase (Figure 8b), indicating that C_6H_{14} and water have begun to mix, similar to the two-phase miscibility characteristics in the PTE in this stage. At 250°C/60 MPa, C_6H_{14} molecules enter the water zone, and the mixing of the two types of molecules at the interface is more intense; the interface is not clearly defined (Figure 8c). At 320°C/80 MPa, the number of both types of molecules increases significantly in the other's zone, and the same molecules tend to coalesce. At this time, the interface is ambiguous (Figure 8d), corresponding to the presence of a water segment in the oil phase in the PTEs under the same *T-P* conditions. At 375°C/95 MPa, the mixing degree of the C_6H_{14} and water molecules close to the interface has increased. More C_6H_{14} molecules have entered the water zone and coalesced, corresponding to the local miscibility and growth of oil droplets in the water phase in the PTE with the same *T-P* conditions (Figure 8e). At 404°C/100 MPa, the width of the interface mutual miscibility of the two molecules increased (Figure 8h). At this time, the interface still exists, but it is very fuzzy (Figure 8f). As the *T-P* increase, the instantaneous configuration and relative concentration show that the two types of molecules are uniformly distributed in the simulation box at 450°C/110 MPa (Figure 8g, 8i).

3.4 C_8H_{18}-H_2O system

In the C_8H_{18}-water system, A few oil droplets are present in the water phase from 25°C/20 MPa (Figure 2a3) to 150°C/20 MPa (Figure 9a1). At 260°C/70 MPa, the C_8H_{18} and water are slightly miscible near the interface (Figure 9a2). At 300°C/80 MPa, the oil droplets in the water phase coalesce and become larger, and the water droplets in the C_8H_{18} phase near the interface move violently (Figure 9a3). Raman signals of the C_8H_{18} and water were obtained at the position of the oil droplet (Figure 9b1). At 375°C/95 MPa, bubbling occurs near the interface, reflecting the active exchange of C_8H_{18} and water (Figure 9a4). At 400°C/100 MPa, a water segment has formed in the oil phase (Figure 9a5). At 410°C/100 MPa, the oil droplets in the water phase and the water droplets in the C_8H_{18} phase coalesce and disperse extensively (Figure 9a6), showing fast and extensive miscibility of oil and water. Finally, at 423°C/105 MPa, the C_8H_{18} and water are completely miscible (Figure 9a7). The Raman signals of C_8H_{18} and water are detected in the miscible liquid (Figure 9b2).

At 150°C/20 Ma in the MDNS, the C_8H_{18}-water system is divided into three parts, including a water zone, interface zone, and pure C_8H_{18} zone. A clear interface exists between the water and C_8H_{18} phases, and only one water molecule is identified in the C_8H_{18} phase, showing the immiscibility of the fluids (Figure S2a). At 260°C/70 MPa, the number of water molecules in the C_8H_{18} phase increases significantly, and the C_8H_{18} molecules pass through the interface and enter the water phase. The C_8H_{18} and water molecules in the interface zone are intensely mixed (Figure S2b), indicating partial miscibility of C_8H_{18} and water near the interface. At 300°C/80 MPa, the C_8H_{18} passes through the interface and enters the water area, and the degree of mixing of the two phases is intensified (Figure S2c). At 375°C/95 MPa, the number of water molecules in the C_8H_{18} zone and the number of C_8H_{18} molecules in the water zone increase, and the mixing of the different types of molecules near the interface are widespread (Figure S2d). This result corresponds to the active oil-water exchange in the form of “bubbling” in the thermal experiments. At 400°C/100 MPa, the number of water molecules in the C_8H_{18} phase and the number of C_8H_{18} molecules in the water phase increase, and the same types of molecules aggregate (Figure S2e). This phenomenon corresponds to the appearance of a water segment in the oil phase in the PTE with the same *T-P* conditions. At 423°C/105 MPa, more water and C_8H_{18} molecules have gathered in the C_8H_{18} zone and water zone, respectively. The interface still exists (Figure S2f), but its width is significantly larger (Figure S2i). The miscibility state of the system differs from that in the PTE. As the *T-P* increases, the instantaneous configuration and the relative concentration curve show that the C_8H_{18} and water molecules are uniformly distributed in the simulation box at 500°C/110 MPa, and the interfaces between the different types of molecules have disappeared (Figure S2h, S2j).

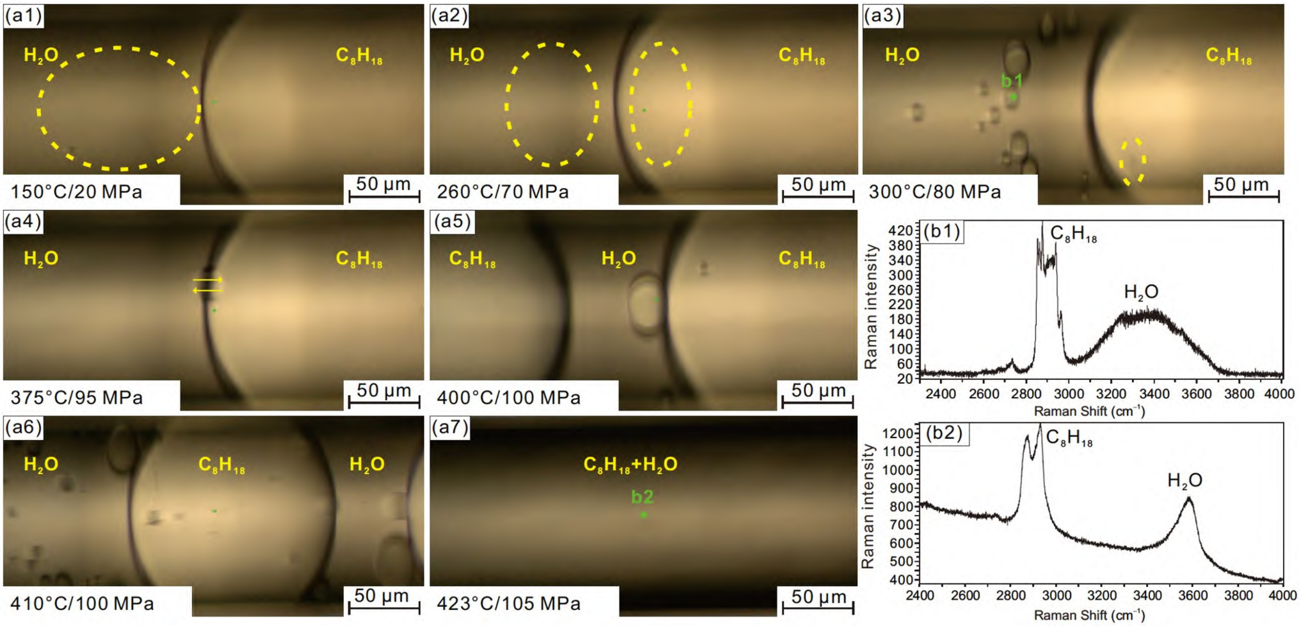

Figure 9 Miscibility features of C_8H_{18}-H_2O system in HTHPOC and *in-situ* Raman spectra.

3.5 C_6H_{14}-CO_2-H_2O system

From 25°C/5 MPa (Figure 2a5) to 25°C/8 MPa (exceeding the CO_2 critical pressure of 7.39 MPa), the interface between C_6H_{14} and CO_2 starts to move violently, indicated by the dynamic circulating stripes in the C_6H_{14} near the interface (Figure 10a1). Then, the C_6H_{14} and CO_2 dissolve into each other rapidly, forming a homogenous C_6H_{14}+CO_2 miscible phase (Figure 10a2). At 25°C/20 MPa, there are many tiny but visible C_6H_{14}+CO_2 beads and a large one in the water near the interface between the miscible C_6H_{14}+CO_2 phase and the water phase (Figure 10a3). The larger bead shows Raman peaks of water, CO_2, and C_6H_{14} (Figure 10b1). The intensity of the CO_2 and C_6H_{14} peaks is very low, and the CO_2 peak is substantially affected by a shift in the baseline. The extremely low peak intensity of C_6H_{14} indicates that only a small amount of C_6H_{14} has entered the water phase with the mixed CO_2. At 50°C/20 MPa, many oil bubbles appear in a large area of the water, small oil bubbles move violently at the interface, and water droplets appear in the C_6H_{14}+CO_2 miscible phase near the interface (Figure 10a4). At 100°C/20 MPa, the water droplets in the C_6H_{14}+CO_2 miscible phase near the interface coalesce and become larger (Figure 10a5). At 150°C/20 MPa, the water droplets in the miscible phase near the interphase coalesce into water sheets (Figure 10a6). At 150°C/30 MPa, several tiny oil bubbles appear in most of the water phase near the interface, and there are large and small oil bubbles in the entire section of the water phase at the closed end of the capillary tube. Fluid flow is observed in a long section of the miscible phase at the right part near the interface (Figure 10a7). At 280°C/80 MPa, all phases near the interface are more active. The oil bubbles in the water near the interface become larger due to continuous convergence and dispersion. It is also observed that large oil bubbles popped out near the interface and enter the middle part of the water phase due to the difference in interface tension. The color difference between the two phases also decreases, blurring the interface between the two phases (Figure 10a8), indicating an increase in the miscibility of the C_6H_{14}+CO_2 phase and water phase. At 300°C/80 MPa, the interface moves rapidly to the left, and only a small section of water remains at the closed end. The C_6H_{14}+CO_2 phase

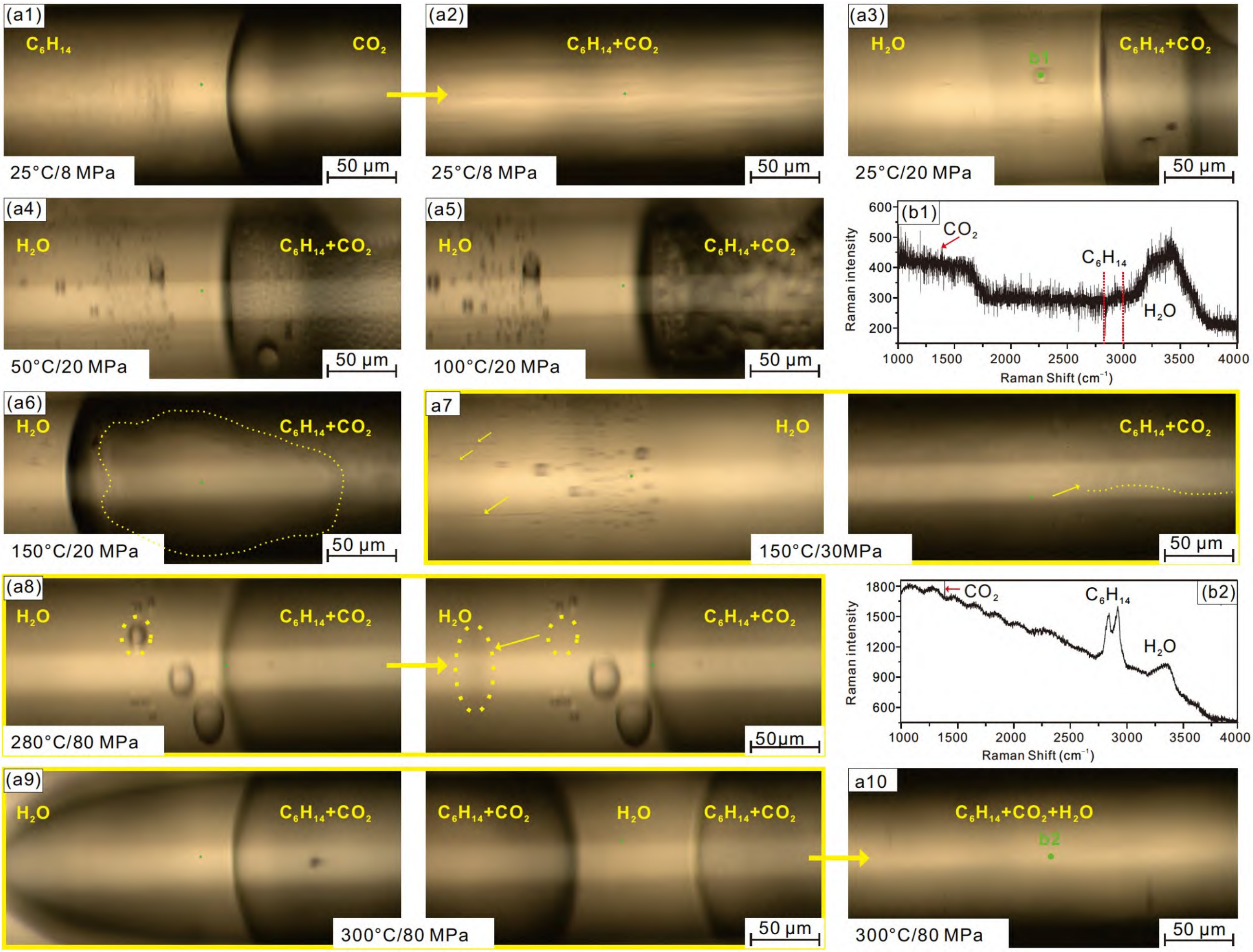

Figure 10 Miscibility features of C_6H_{14}-CO_2-H_2O system in the HTHPOC and *in-situ* Raman spectra.

"extrudes" water from the closed end during the mixing process, causing the water phase to coalesce from water segments in the C_6H_{14}+CO_2 phase (Figure 10a9). At this time, the C_6H_{14}+CO_2 phase and the water phase are partially miscible segmentally. The length of the water segments in the C_6H_{14}+CO_2 phase decreases and lastly disappears, resulting in complete miscibility of the three phases (Figure 10a10). The Raman peaks of CO_2, C_6H_{14}, and water are detected in the mixed liquid phase after complete miscibility (Figure 10b2).

In the MDNSs, the C_6H_{14}-CO_2-water system at 25°C/8 MPa can be divided into seven parts, including two water zones, a CO_2 zone, a C_6H_{14} zone, and three interfaces between each of the two phases. Due to the dissolution of a large amount of CO_2 into the C_6H_{14} phase, the C_6H_{14} region expands in the equilibrium process under this condition. Many C_6H_{14} molecules enter the CO_2 phase, resulting in a much wider area of the interface between CO_2 and C_6H_{14}, and the division is far less clear than at 25°C/5 MPa (Figure 11a). There are clear interfaces between the water and the CO_2 and C_6H_{14} phases on both sides, respectively. A small amount of CO_2 enters the water zone on both sides, and the number of CO_2 molecules entering the water is higher on the left side, where the water is in direct contact with the CO_2, than on the right side where the water is in direct contact with C_6H_{14}. CO_2 accumulates at the right interface between the water and the C_6H1_4. On the left side, a few water molecules enter the adjacent CO_2 phase. However, on the right side, water molecules only enter the C_6H_{14} region (Figure 11a). At 25°C/20 MPa, the miscibility state of the system exhibits little change, but the interface width between the water on both sides and the CO_2 and C_6H_{14} phases and between the CO_2 and C_6H_{14} phases is slightly larger, and the miscibility degree of the two phases is larger than in the previous condition (Figure 11b). At 150°C/20 Ma, the CO_2 and C_6H_{14} are fully mixed, and most of the C_6H_{14} has mixed with the CO_2, resulting in a significant increase in the miscibility of the two phases. The number of CO_2 molecules in the water has increased on both sides, and the number of water molecules in the CO_2 phase adjacent to the left-side water has increased significantly. They are miscible with C_6H_{14} molecules that have also mixed in the CO_2 phase. The water on the right side adjacent to the local CO_2+C_6H_{14} miscible phase show an increase in the miscibility degree in the interface area, and a few water molecules have entered the adjacent CO_2+C_6H_{14} miscible phase (Figure 11c). At 210°C/40 MPa, the CO_2 molecules on both sides of the water zone have increased significantly, and more water molecules have entered the middle zone. A few C_6H_{14} molecules pass through the boundary and enter the water on both sides. CO_2 and C_6H_{14} are almost completely miscible in the instantaneous configuration (Figure 11d). In contrast, the relative concentration curves show that CO_2 and C_6H_{14} are not completely miscible at this time (Figure 11j). At 250°C/60 MPa, the relative concentration curve shows that the CO_2 and C_6H_{14} are completely miscible in the middle of the system (Figure 11j). The amount of CO_2 in the water on both sides has also increased significantly, indicating a H_2O+CO_2 miscible phase on both sides. The C_6H_{14} molecules entering the H_2O+CO_2 miscible phase have increased slightly, especially on the left side. The water molecules on both sides have entered the middle CO_2+C_6H_{14} phase, and there is a tendency for aggregation of the water molecules, which can be regarded as the beginning of the segmental miscibility stage (Figure 11e). At 320°C/80 MPa, the number of C_6H_{14} molecules entering the H_2O+CO_2 phase continues to increase, and the number of water molecules entering the CO_2+C_6H_{14} phase increases significantly, but the interface still exists between the two miscible phases (Figure 11f). As the *T-P* increase, the CO_2+C_6H_{14} miscible phase continuously diffuses to both sides, and more water molecules enter it from both sides. The interface between the two miscible phases becomes blurred (Figure 11g, 11h). Finally, at 430°C/105 MPa, no fluctuations are observed in the relative concentration curves of the single-component and multi-component systems. All interfaces in the C_6H_{14}-CO_2 water system have disappeared, and the entire three-phase system is completely miscible (Figure 11i, 11k).

3.6 C_8H_{18}-CO_2-H_2O system

From 25°C/5 MPa (Figure 2a6) to 25°C/8 MPa, intense activity is observed near the interface between the C_8H_{18} and CO_2 (Figure 12a1), and the two fluids rapidly form a C_8H_{18}+CO_2 miscible phase (Figure 12a2). The Raman peaks of CO_2 and C_8H_{18} were obtained on the right and left sides of the C_8H_{18}+CO_2 miscible phase. The relative intensity of the C_8H_{18} Raman peak is significantly higher on the left side than on the right side (Figure 12b1, 12b2), indicating that the miscible C_8H_{18}+CO_2 phase is not homogeneous at this stage. At 25°C/20 MPa, the fluctuations near the initial interface expand on both sides and the miscible phase section stabilizes. Very small but visible oil-gas beads appear in the water phase near the interface (Figure 12a3). At this time, water, CO_2, and C_8H_{18} Raman peaks (Figure 12b3) are detected in the water phase on the left side of the interface. The C_8H_{18} peak intensity is extremely low, indicating that a large amount of CO_2 enters the water, but only a little C_8H_{18} is mixed into the water with the CO_2. At 50°C/20 MPa, numerous oil bubbles appear in a wide range of the water phase. The small oil bubbles move violently at the interface, and water droplets appear near the interface in the C_8H_{18}+CO_2 miscible phase (Figure 12a4). In addition to the Raman peaks of CO_2 and C_8H_{18}, the peak occurs at 3630.68 cm^{-1} (Figure 12b4), representing H_2O or OH formed in the quartz during the heating process. The Raman features indicate that the

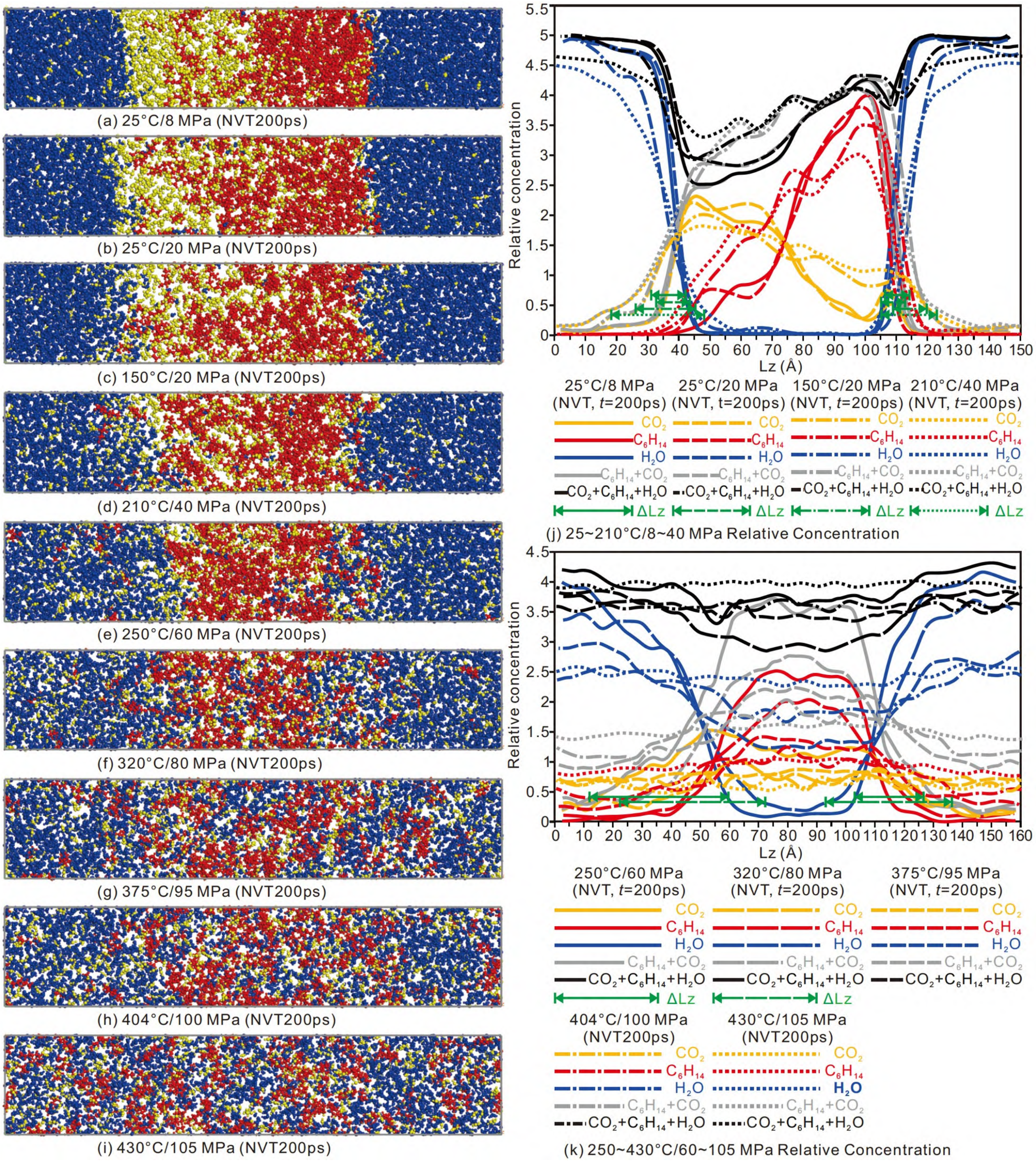

Figure 11 Instantaneous configurations and relative concentration curves of the C_6H_{14}-CO_2-H_2O systems in the MDNSs.

amount of CO_2 and C_8H_{18} in the water phase is much larger than the amount of water in the miscible phase, and the C_8H_{18} +CO_2 phase and water phase are partially miscible. At 100°C/20 MPa, the water droplets within a certain range of the C_8H_{18}+CO_2 miscible phase near the interface aggregate and become larger, and the existing C_8H_{18}+CO_2 phase has accumulated at the closed end, replacing the water (Figure 12a5). *In-situ* Raman detection was carried out on the oil bubbles in the water on the right side near the interface. Raman peaks of CO_2, $C_8H_{18,}$ and water were observed (Figure 12b5). At 150°C/20 MPa, the water droplets in the C_8H_{18}+CO_2 miscible phase near the interface coalesce into water sheets (Figure 12a6). At 170°C/30 MPa, the fluid flows into the C_8H_{18}+CO_2 miscible phase far away from the interface between the water and C_8H_{18}+CO_2 miscible phases (Figure 12a7). At 210°C/40 MPa, a small water segment

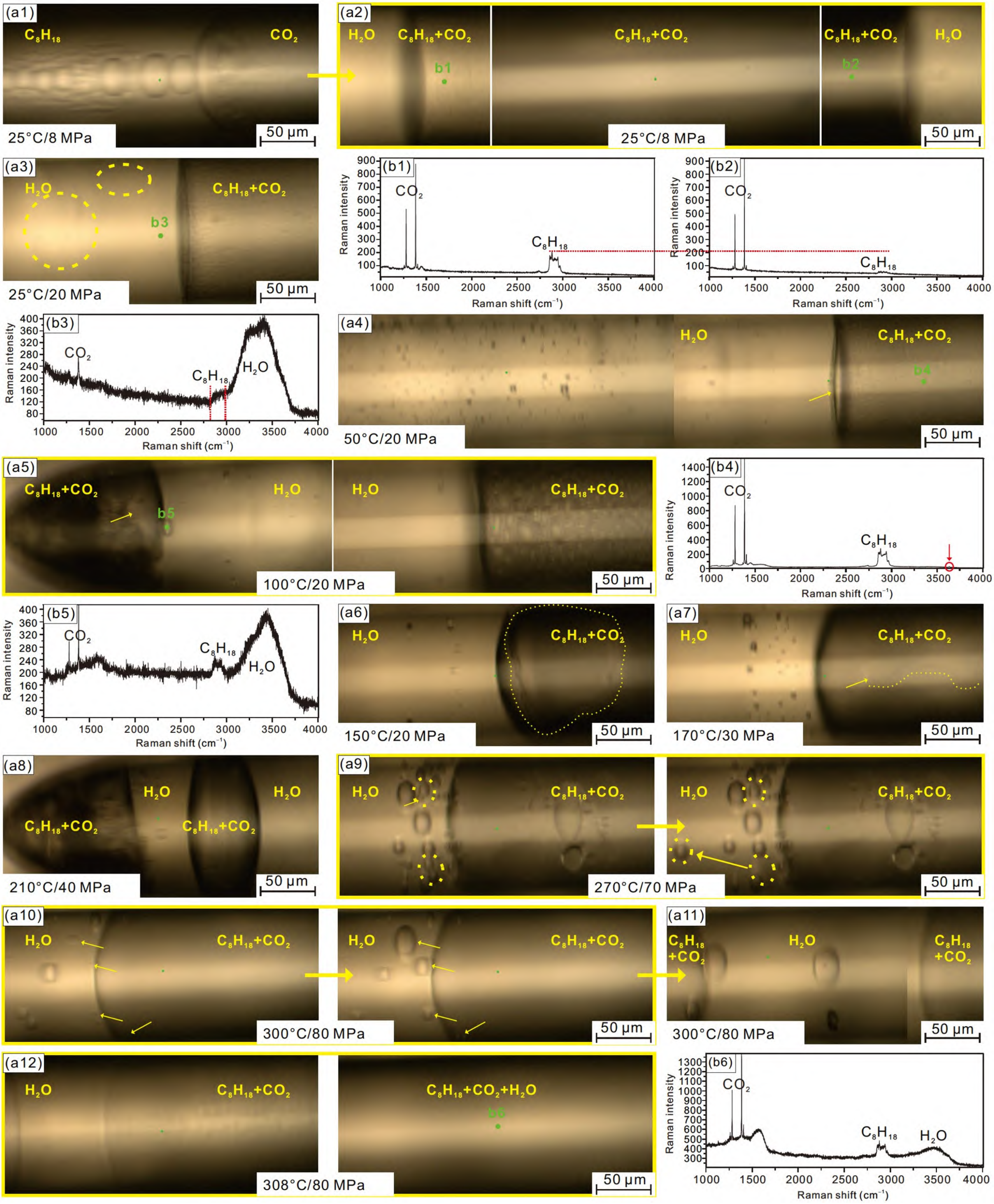

Figure 12 Miscibility features of C_8H_{18}-CO_2-H_2O system in the HTHPOC and *in-situ* Raman spectra.

forms in the $C_8H_{18}+CO_2$ phase at the top of the closed end (Figure 12a8). At 270°C/70 MPa, bubbling occurs near the interface, indicating an active exchange between the oil/gas and water phases, and the oil bubbles in the water become larger due to rapid and continuous aggregation and dispersion. It is also observed that the larger oil bubbles are ejected into the middle part of the water phase from the interface due to the difference in interface tension, and the interface moves to the left side (Figure 12a9). At 300°C/80 MPa, the phases near the interface are more active. The bubbling speed at the interface is faster, and the oil bubbles in the water aggregate and disperse quickly (Figure 12a10). The interface moves quickly to the left towards the closed end and finally disappears. The water forms segments in the C_8H_{18}+CO_2 phase that contain oil bubbles (Figure 12a11). At this time, the C_8H_{18}+CO_2 phase and the water phase are in the segmentally dynamic miscibility stage. The color difference between the different phases is significantly lower, indicating increased miscibility of the C_8H_{18}+CO_2 phase and water phase. At 308°C/80 MPa, the interface between the C_8H_{18}+CO_2 phase and the water phase moves violently. The interface blurs rapidly, the C_8H_{18}+CO_2 phase on both sides of the water segments rapidly dissolves with the water, and the water segments shorten until they disappear. Finally, complete miscibility of the three phases is achieved (Figure 12a12). Raman peaks of CO_2, C_8H_{18}, and water are detected (Figure 12b6).

In the MDNSs, the system at 25°C/8 MPa can be divided into seven parts, similar to the C_6H_{14}-CO_2 water system. The miscibility state is also similar to the C_6H_{14}-CO_2-water system under the same conditions, except that there are fewer CO_2 molecules in the C_8H_{18} zone, and only a few C_8H_{18} molecules in the CO_2 zone (Figure S3a). At 25°C/20 MPa, the miscibility state of the system does not change much, but the interface width between the water on both sides and the CO_2 and C_8H_{18} are slightly larger, whereas the interface width between the CO_2 and C_8H_{18} is slightly smaller (Figure S3b). This likely reason is that when only the pressure increases, the volume of the liquid alkane is significantly compressed, and the pressure far exceeds the critical pressure of CO_2 and is close to the critical pressure of water. Therefore, the CO_2 is near the supercritical state and has a strong diffusion capacity, whereas the volume of liquid water is not affected. At 150°C/20 MPa, the CO_2 is fully mixed with the C_8H_{18} phase, the C_8H_{18} is largely mixed with the CO_2, and the miscibility degree between the two phases has increased significantly. The amount of CO_2 in the water has increased on both sides, and the number of water molecules in the CO_2 adjacent to the water on the left-side has increased significantly. They are miscible with the C_8H_{18} molecules in the CO_2 phase. The miscibility degree between the water on the right side and the adjacent C_8H_{18}+CO_2 miscible phase is higher only in the interface zone, and only a few water molecules enter the local C_8H_{18}+CO_2 miscible phase (Figure S3c).

At 260°C/70 MPa, the CO_2 in the middle of the system is completely miscible with the C_8H_{18}, and the CO_2 in the water on both sides has increased significantly. The two sides can be regarded as H_2O+CO_2 miscible phases. A few C_8H_{18} molecules enter the H_2O+CO_2 miscible phase, and the water on both sides is partially miscible with the C_8H_{18}+CO_2 phase. In addition, the water molecules begin to coalesce, but interfaces remain between the middle C_8H_{18}+CO_2 phase and the H_2O+CO_2 miscible phase on both sides (Figure S3d). At 300°C/80 MPa, the interface remains between the two miscible phases. The amount of C_8H_{18} entering the H_2O+CO_2 phase increases slightly, whereas the amount of water entering the C_8H_{18}+CO_2 phase increases significantly, and it accumulates at multiple locations (Figure S3e). This phenomenon corresponds to the state when water segments begin to appear in the miscible phase at 220°C/45 MPa in the thermal experiments. As the *T-P* increases, the C_8H_{18}+CO_2 miscible phase diffuses into the water phase on both sides, and more water molecules are mixed into the C_8H_{18}+CO_2 miscible phase. The interface between the two miscible phases becomes blurred (Figure S3f, S3g, S3h). Finally, at 450°C/110 MPa, no fluctuations are observed in the relative concentration curves of the single-component and multi-component systems. All interfaces in the C_8H_{18}-CO_2-water systems have disappeared, and the three phases are completely miscible (Figure S3i, S3k).

The results show that only the CH_4-water systems exhibit the same mixing processes and features in the MDNSs and visual PTEs. In the other five systems, higher temperatures are required in the MDNSs than in the PTEs to reach the same miscibility degree in the HTHP stage. This finding indicates that the HTHP MDNS of complex fluids still requires more constraints from HTHP PTEs.

4. Discussion

4.1 Effect of *T-P* on miscibility

The results of the PTEs in the alkane-H_2O systems and alkane-CO_2-H_2O systems from LTLP to HTHP show that, the miscibility degree of the organic and inorganic fluids in all systems increases with an increase of temperature and pressure, and complete miscibility is achieved under specific *T-P* conditions (Figures 6, 7, 9, 10, and 12). We analyzed the instantaneous configuration diagrams obtained from the MDNSs, and the relative concentrations of the individual components and multiple components obtained (Figures 5, 8, 11; Figures S1–S3). The average widths of the interfaces in different systems with various temperatures and pressures (Table 2) were obtained following the "10–90" principle (Yuet and Blankschtein, 2010; Zhao et al., 2011). The evolution of the average width of the interfaces with increased *T-P* was obtained for the four types of alkane-H_2O systems and two types of alkane-CO_2-H_2O systems (Figure 13). Although there are some differences in the growth rate of the interface width in different systems, the average width of the miscibility interface between different phases increases with an increase in temperature and pressure, indicating an increase in the miscibility degree. In addition, the growth rate increases exponentially. A comparison of the curves of dif-

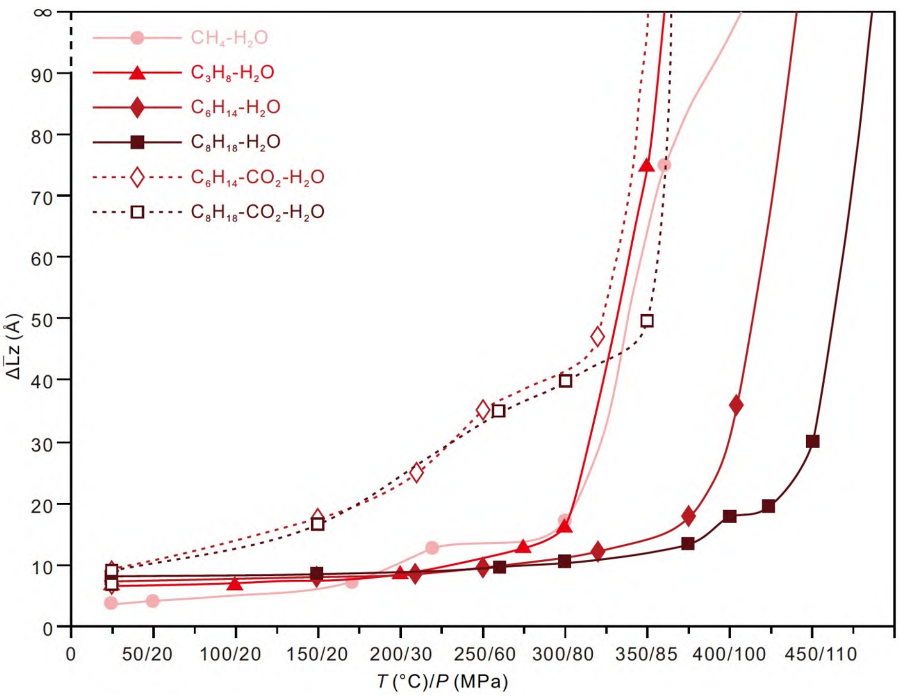

Figure 13 The change in the average interface width during the mixing process of fluids in the alkane-water and alkane-CO_2-water systems as the *T-P* increase. The pressure *P* corresponding to the temperature *T* is the same as listed in Table 2; ∞ represents a value infinitely close to the *x*-direction of the system's simulation box under the temperature and pressure conditions

ferent systems shows an inflection point in the curves of the interface width in the alkane-H_2O system, indicating a sudden change in growth rate. The change in the growth rate of the interface width is not as significant for the alkane-CO_2-H_2O systems as for the alkane-H_2O system. In the early slow growth stage, the increase rate of the interface width is higher for the alkane-CO_2-H_2O systems than for the alkane-H_2O systems, and the late fast growth stage occurs earlier in the alkane-CO_2-H_2O systems than in the alkane-H_2O systems.

In general, the miscibility degree between different phases in the geological systems increases as the *T-P* increase. The reason may be that the temperature will accelerate the thermal movement of molecules, increasing the distance between the molecules and the self-diffusion coefficient, and thus promoting its movement and diffusion (Wang, 2014; Zhang et al., 2015). Essentially, the temperature increase causes the breaking of hydrogen bonds, enabling the entrance of other molecules into the water and increasing the solubility of alkanes in water (Dubessy et al., 1999).

4.2 Effect of the carbon number on miscibility

First, Figure 13 shows that the differences in the average interface width between different alkane-water systems are relatively small and do not exceed 10 Å in the initial 200 ps of the simulation under relatively LTLP conditions (155–210°C). However, the interface width increases slightly as the carbon number increases, indicating that alkanes with more carbon atoms have higher miscibility with water under LTLP conditions. After exceeding this LTLP, the average interface width between C_3H_8 and water is larger than that between CH_4 and water when the *T-P* exceed 300°C/80 MPa, indicating that the mutual solubility is higher between water and gaseous alkanes with more carbon atoms than between water and gaseous alkanes with fewer carbon atoms under HTHP conditions. Under HTHP conditions exceeding 300°C/80 MPa, the average interface width between C_6H_{14} and water increases faster than that between C_8H_{18} and water, indicating that the miscibility of water and liquid alkanes with fewer carbon atoms is higher than that of water and liquid alkanes with more carbon atoms.

Second, Figure 14 shows that the *T-P* required for achieving the initial mixing and segmentally dynamic mixing increases with an increase in the carbon number, in the PTEs and MDNSs. In the PTEs, the *T-P* required for complete miscibility of water and C_3H_8, C_6H_{14}, CH_4, and C_8H_{18} increases successively, and the required *T-P* are similar for C_6H_{14} and CH_4. In the MDNSs, the *T-P* required for complete miscibility of water and C_3H_8, CH_4, C_6H_{14}, and C_8H_{18} increase successively.

To sum up, the miscibility of different phases in the alkane-(CO_2)-water systems decreases with an increase in the carbon number of alkanes, and only two gaseous alkane-water systems show differences in the complete miscibility stage. The reason is that an increase in the carbon number, i.e., an increase in the chain length, increases the molecular volume,

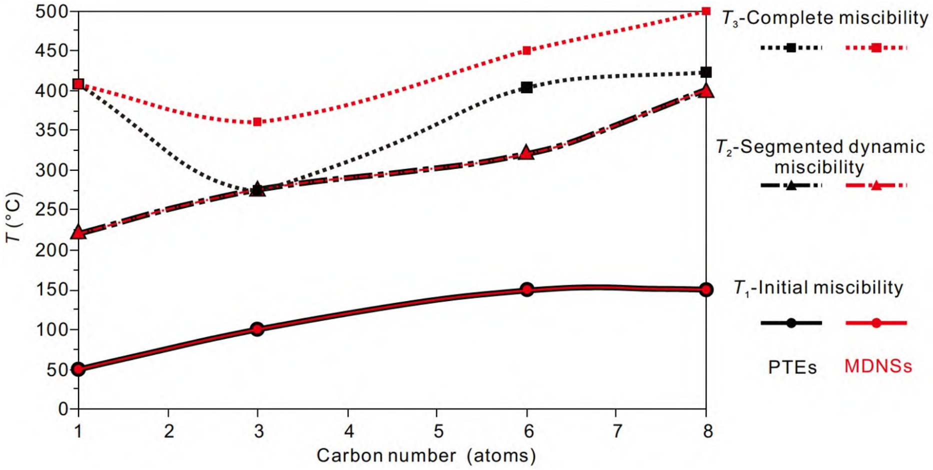

Figure 14 Temperature and pressure versus carbon number at different mixing stages of the alkane-H_2O systems. The pressure P corresponding to temperature T is the same as in Table 2.

slowing the diffusion of molecules (Wang, 2010). In addition, the van der Waals interaction energy between alkanes and CO_2 and the dispersion force that plays a fundamental role also decreases with an increase in the alkane chain length (Wang, 2014; Zhang et al., 2015). In addition, the volumetric expansion coefficient of the alkanes decreases with an increase in the chain length (Li et al., 2006; Yang et al., 2012).

4.3 Effect of CO_2 bridge function on the miscibility of alkanes and water

The required *T-P* conditions for the three mixing stages (initial mixing, dynamic mixing, and complete mixing) of the C_6H_{14}/C_8H_{18}-water and C_6H_{14}/C_8H_{18}-CO_2 water systems are shown in Figure 15. The results show that the *T-P* required for the alkane-CO_2-water systems to achieve the three different mixing stages are significantly lower than those of the alkane-water systems without CO_2, indicating that CO_2 acts as a bridge between the alkanes and water and promotes the miscibility of alkanes and water. The increase rate of the alkane-water interface width is significantly higher in the system with CO_2 than in the system without CO_2 (Figure 13), also suggesting the bridge function of CO_2.

The bridge function is directly related to the characteristics of near-critical and supercritical CO_2 under HTHP conditions and is reflected in the microscopic miscibility of the three-phase systems. The reason for this bridge function is two-fold. First, a large number amount of near-critical and supercritical CO_2 and alkanes in the system is mixed in the relatively low-medium temperature stage (Figures 10, 12a1–12a4; Figure 11a–11b; Figure 3a–3b). The C-C interaction of short-chain alkanes is weaker than the C-CO_2 interaction of alkanes and CO_2, thus, the alkanes are easily dissolved and diffuse rapidly into supercritical CO_2. Another reason may be that the dispersion force in the van der Waals force (the dispersion force refers to the weak attraction between the instantaneous dipole moments of molecules when they are close to each other) may be critical for the mixing of alkanes and CO_2 (Wang, 2014; Zhang et al., 2015). Second, a large amount of CO_2 is dissolved in water as the *T-P* rise (Figure 11b–11d; Figure S3b–S3d). The CO_2 dissolved in water readily combines with alkanes, forming a favorable miscible channel between the mixed phases of alkane-CO_2 (Figure 11d–11i; Figure S3d–S3i) and the mix phases of water-CO_2. In addition, the accumulation of CO_2 molecules near the alkane side at the interface between the alkane and water in the initial stage of the alkane-CO_2-water system may be caused by a difference in the interfacial tension between alkane-CO_2, alkane-water, and CO_2-water.

4.4 Miscibility processes and patterns

4.4.1 Miscibility processes and patterns of the alkene-water systems

The PTEs and MDNSs show that the mixing of different types of alkanes with water is significantly affected by the *T-P* from TLP to HTHP conditions. We propose a mixing model of the fluids in the alkane-water systems consisting of seven stages based on the real-time observations of the mixing of fluids in the four alkane-water systems with increased *T-P* obtained from the PTEs and the comparative analysis of the MDNS result at different temperatures and pressures (Figure 16).

(1) Immiscibility stage. A clear interface exists between the alkane and water, and the system is divided into three parts: a water zone, an interface zone, and an alkane zone (Figure 16a).

(2) Initial partial miscibility of alkanes and water near the interface. Tiny water droplets and oil droplets are observed in the alkane and water phases near the interface in the PTEs. In the MDNSs, the water and alkane molecules entered the

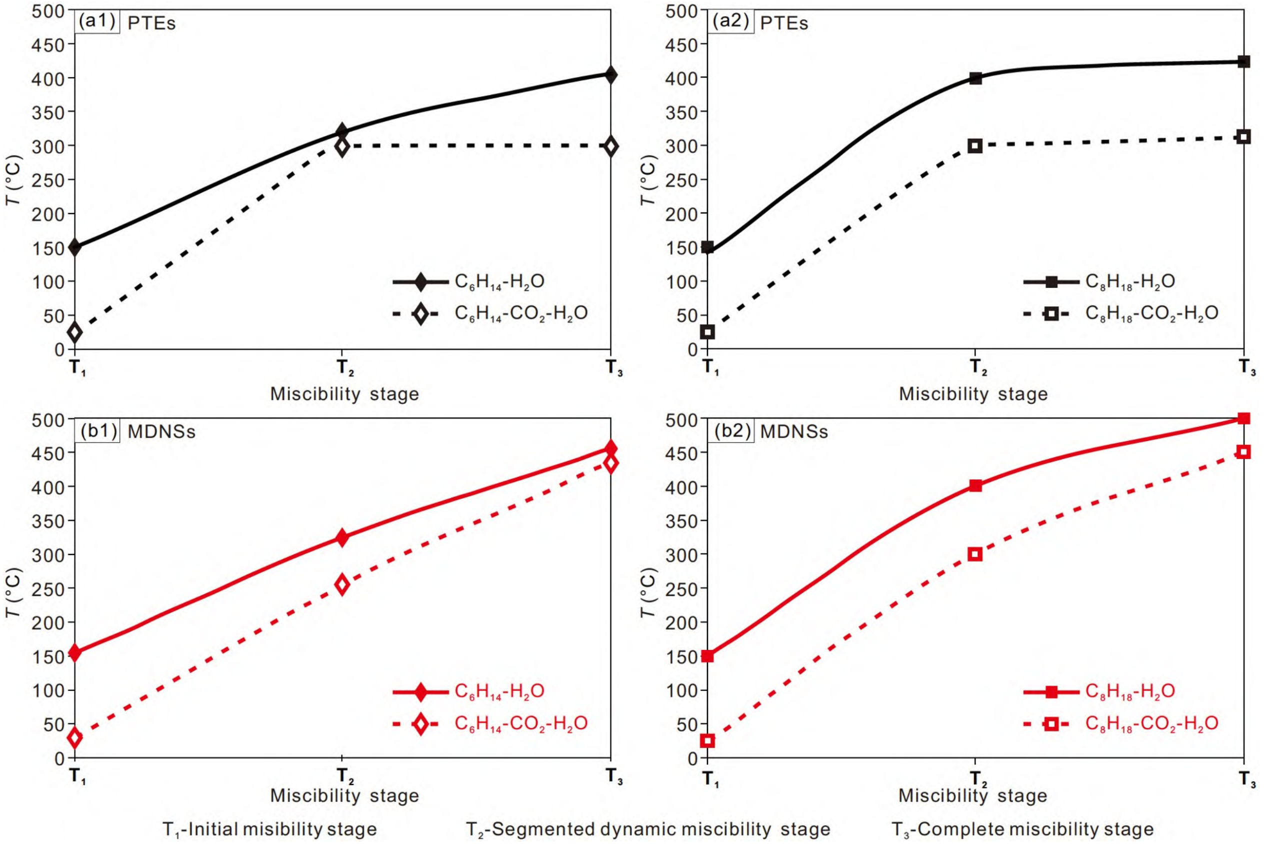

Figure 15 Comparison of temperature and pressure required in each miscibility stage of the C_6H_{14}/C_8H_{18}-H_2O and C_6H_{14}/C_8H_{18}-CO_2-H_2O systems in thermal experiments and dynamic simulations. The pressure *P* corresponding to temperature *T* is the same as in Table 2; The pressure corresponding to T1 (25°C) of the C_6H_{14}-CO_2-H_2O and C_8H_{18}-CO_2-H_2O systems is 20 MPa.

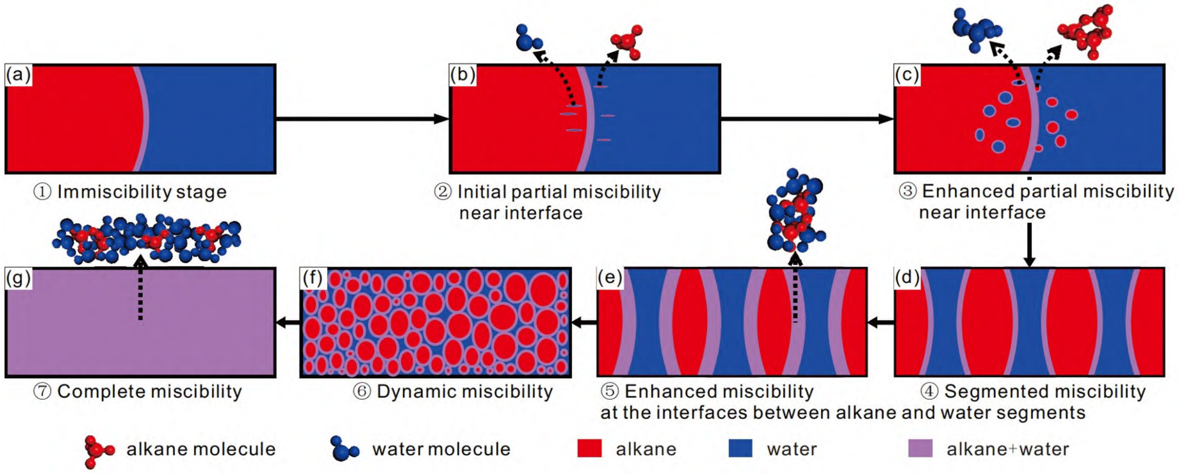

Figure 16 Models of the miscibility of the fluids in the alkane-water systems from LTLP to HTHP.

alkane and water zones near the interface, respectively (Figure 16b).

(3) Enhanced partial miscibility of alkanes and water near the interface. The size of the water droplets and oil droplets in the oil and water phases within a certain range near the interface increase in the PTEs. The MDNS results show the aggregations of the same molecules in the other fluid phase (Figure 16c).

(4) Segmented miscibility of alkanes and water. The alkane and water droplets coalesce to form segments of alkene and water in the PTEs, and the alkene/water segments become shorter with the continued aggregation and dispersion. The MDNS results show the aggregation of the same type of molecules (Figure 16d).

(5) Enhanced miscibility at the interfaces between the alkane and water segments. The local miscible zones between the alkane and water segments become wider. The MDNSs indicate that the interface is blurring due to the gradual mixing of different molecules (Figure 16e).

(6) Dynamic miscibility of alkanes and water. After reaching a certain *T-P* in the PTEs, the alkane and water phases reach a stage of dynamic circulation of miscibility and separation. In the MDNSs, this stage is represented by the alternating dispersion and aggregation of the same molecules as the simulation continues at specific *T-P* conditions (Figure 16f).

(7) Complete miscibility of alkanes and water. The system reaches a stable homogeneous phase. In the MDNSs, the interfaces between different molecules disappear and the same molecules are uniformly distributed in the simulation box (Figure 16g).

4.4.2 Miscibility processes and patterns of the alkene-CO_2-water systems

Similarly, the miscibility of the fluids in different alkane-CO_2-water systems is also affected by the *T-P*. The mixing model of the alkane-CO_2-water systems from LTLP to HTHP conditions can be divided into the following eight stages (Figure 17).

(1) Immiscibility stage. The CO_2, alkanes, and water are immiscible, and there are interfaces between the components. The fluid systems can be divided into CO_2 zone, alkane zone, pure water zone, and interfaces, and no clear miscibility occur near the interfaces (Figure 17a).

(2) Partially miscibility of alkane/CO_2 and initial miscibility of water/CO_2. The CO_2 and alkanes are partially miscible as CO_2 diffuses into the alkanes. CO_2 and water begin to mix, and very few micro water droplets and gas bubbles are present near the interface between CO_2 and water. The MDNS shows numerous CO_2 and alkane molecules distributed commonly in the initial alkane zone. There are individual CO_2 molecules entering the water near the interface on both sides, with more on the left side than on the right side. Some water molecules are also observed in the CO_2 zone near the interface (Figure 17b).

(3) Complete miscibility of alkanes/CO_2 and partial miscibility of water/CO_2. CO_2 in the central zone is completely miscible with alkanes, forming the alkane+CO_2 phase. The miscibility degree of CO_2 and water has increased in the system, especially in the part with direct contact between the two phases. The MDNS shows the mixing of alkane and CO_2 molecules in the initial alkane and CO_2 zones. CO_2 molecules enter the water near the interface on both sides, with more on the left side than on the right side. More water molecules enter the CO_2 zone near the interface (Figure 17c).

(4) Forming of H_2O+CO_2 phase via miscibility of CO_2 and water, and initial miscibility of H_2O+CO_2 phase and alkane +CO_2 phase. CO_2 dissolves completely in the alkane and water phases, forming alkane+CO_2 and H_2O+CO_2 miscible phases that begin initial miscibility. The water droplets

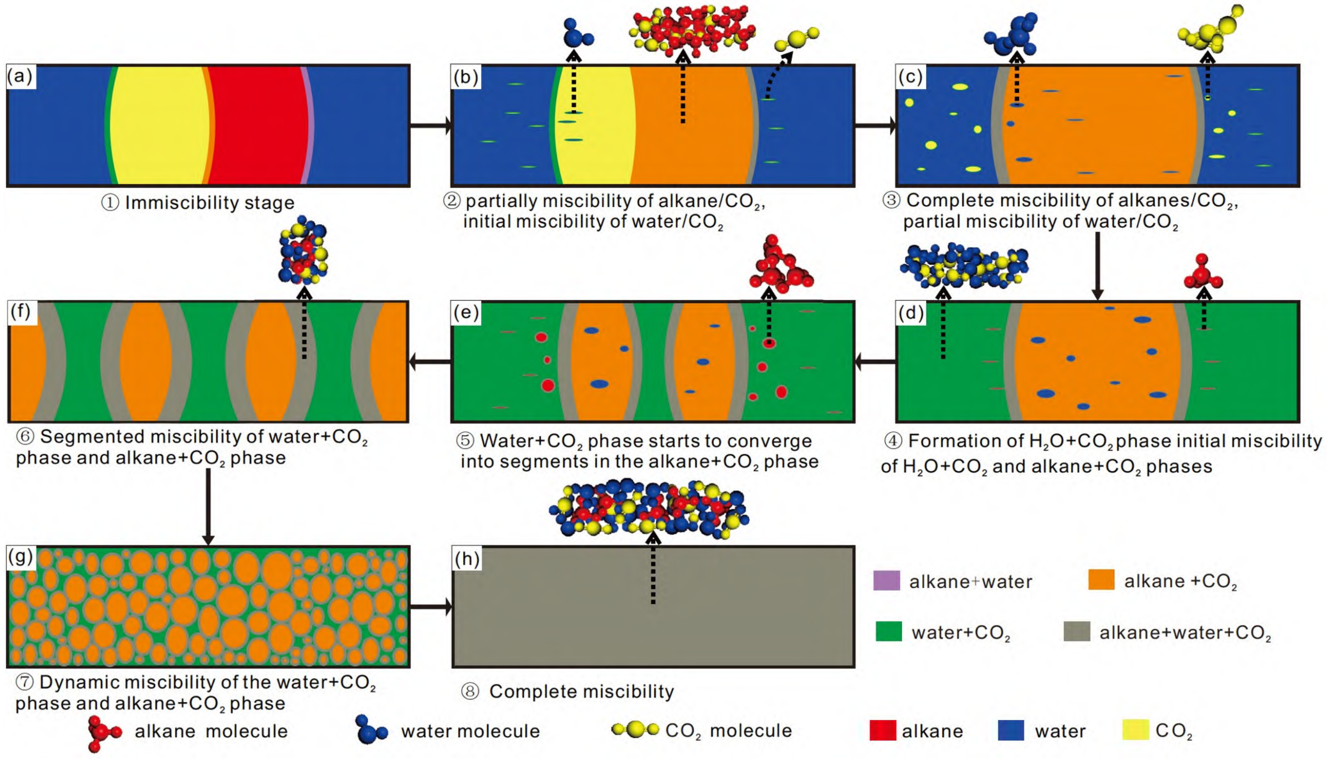

Figure 17 Models of the miscibility of the fluids in the alkane-CO_2-water systems from LTLP to HTHP.

converge in the alkane+CO_2 phase and become larger. A few tiny oil droplets begin to appear in the H_2O+CO_2 phase on both sides. The MDNS shows that CO_2 mix with both the alkane and water. Water molecules enter the alkane+CO_2 phase, and alkane molecules enter the H_2O+CO_2 phase (Figure 17d).

(5) The water+CO_2 phase starts to converge into segments in the alkane+CO_2 phase. The water+CO_2 enters the alkane +CO_2 phase and starts to coalesce to form the water+CO_2 segment. Oil droplets in the CO_2+water phase on both sides gradually become larger. The MDNS indicates a large amount of CO_2+H_2O aggregate in the alkane+CO_2 phase, and the alkane molecules are accumulating in the CO_2+water phase near the interfaces on both sides (Figure 17e).

(6) Segmented miscibility of the water+CO_2 phase and alkane+CO_2 phase. Segments of the water+CO_2 phase and alkane+CO_2 phase exist alternatively. Local mixing occurs at the interfaces between the two miscible phases, and the interface widens. In the MDNS, the water and CO_2, and the alkane and CO_2 coalesce respectively. The same type of molecules aggregates at the interface between the two miscible phases (Figure 17f).

(7) Dynamic miscibility of the water+CO_2 phase and alkane+CO_2 phase. When the required *T-P* conditions have been reached, the two phases become miscible instantaneously, and dynamic miscibility is observed. The MDNS shows that dispersion and aggregation of different types of individual molecules in the water+CO_2 and alkane +CO_2 occur alternately at the same *T-P* conditions (Figure 17g).

(8) Complete miscibility of CO_2, alkanes, and water. The fluids in the system reach a stable homogeneous phase. In the MDNS, the interfaces between different phases have disappeared, and the same molecules are uniformly distributed in the simulation box (Figure 17h).

4.5 Geological significances

The results of this study show that the miscibility of different organic and inorganic fluids is not instantaneous, from LTLP to HTHP conditions. Instead, the miscibility degree increases as the *T-P* increase and different miscibility stages occur. Petroleum, gas, and water exist commonly in the HTHP reservoirs in deep and ultra-deep layers in petroliferous basins (Helgeson et al., 1993; Lewan, 1997; Seewald, 2003; Yuan et al., 2019, 2022; Cao et al., 2022b). In the HTHP ranges (generally less than 200°C) of recently explored deep and ultra-deep reservoirs, most hydrocarbons are partially but not completely miscible with water. A heterogeneous fluid system with incomplete miscibility can promote the formation of different types of fluid inclusions, such as hydrocarbon inclusions, hydrocarbon-bearing aqueous inclusions, and aqueous inclusions in the same diagenetic stages (Ramboz et al., 1982; Chen et al., 2009, 2011; Liu et al., 2017; Chi et al., 2021). Therefore, a wide range of homogenization temperatures exists for different types of fluid inclusions captured in the same diagenetic stage, and there is usually a difference between the homogenization temperature and the capture temperature (Ramboz et al., 1982; Chi et al., 2021; Yang et al., 2022; Zhang et al., 2022).

Besides hydrocarbons and pore water, the hydrocarbon reservoirs in ultra-deep layers of petroliferous basins generally contain some CO_2, especially in the background with the development of deep crust/mantle-derived CO_2 (Smith and Ehrenberg, 1989; Seewald, 2003; Liu et al., 2017, 2019). Under HTHP conditions, the miscibility of hydrocarbon, water, and CO_2 probably has a profound impact on the generation, migration, and preservation of oil and gas. On the one hand, the existence of deep high-temperature pore water (especially the intrusion of large-scale high-temperature thermal fluid) and its mixing with organic matter, can provide heat and hydrogen for the occurrence of the organic-inorganic hydrocarbon generation processes, which can expand the "oil generation window", and promote the generation of more low-molecular-weight hydrocarbons (Liu, 2022). On the other hand, supercritical CO_2 in deep layers can effectively extract hydrocarbons and promote the migration of hydrocarbons from source rocks to reservoirs. The bridging role of CO_2 promotes partial or dynamic miscibility of oil and pore water under relatively lower temperature and pressure conditions in deep layers, effectively reduces capillary resistance at narrow throats in the tight rocks, and promotes efficient migration of hydrocarbon fluid from source rocks to the reservoir. The crude oil associated with CO_2 usually contains more light oil components (Liu et al., 2017, 2019; Zhu et al., 2018; Liu, 2022). In addition, under the HTHP conditions, hydrocarbons in ultra-deep reservoirs are miscible with water, leading to the occurrence of extensive organic-inorganic interactions, which has an important impact on hydrocarbon preservation and reservoir quality. The bridge function of CO_2 increases the miscibility degree of hydrocarbons and water, which can inhibit the asphaltation of hydrocarbons, and promote oil cracking to form more low-molecule weight hydrocarbons and water oxidation of hydrocarbons to form more acids under HTHP conditions (Seewald, 2003). The water oxidation of hydrocarbons generates more CO_2 and increases the miscibility degree of hydrocarbons and water. It can also promote the dissolution of minerals to generate more secondary pores, improving the quality of hydrocarbon reservoirs (Yuan et al., 2019, 2022; Jin et al., 2022).

This study investigated the mixing processes and miscibility patterns of n-alkanes, water, and CO_2 from a perspective of a high geothermal gradient using microscopic *in situ* thermal experiments and molecular dynamics simulations. Research method for studying the miscibility of complex fluid under HTHP is established, and the results provide crucial information for our understanding of the behavior of geofluids. Different petroliferous basins in different areas have very different geothermal gradients. For example, in addition to the hot basins in East China with high geothermal gradients, there are also cold basins with low geothermal gradients and overpressure in West China. In addition, the composition of oil and gas is complex in hydrocarbon reservoirs. Besides normal alkanes, aromatic hydrocarbons and iso-alkanes with different properties are present. Their miscibility with water and CO_2 will affect the miscibility of hydrocarbons with water and CO_2, which still requires further research.

5. Conclusions

(1) The miscibility of fluids in different alkane-H_2O and alkane-CO_2-H_2O systems is not instantaneous from LTLP to HTHP conditions. Instead, the miscibility processes can be divided into three stages, including initial partial miscibility near the interface, segmented dynamic miscibility, and complete miscibility. Further, the mixing of fluids in the alkane-H_2O and alkane-CO_2–H_2O systems can be subdivided into seven and eight mixing stages, respectively.

(2) The temperature significantly affects the miscibility of alkanes, H_2O, and CO_2 in hydrocarbon reservoirs. As the temperature increases, the miscibility of alkanes, H_2O, and CO_2 increases, and the width of the interface between the alkane and water phases increases exponentially. The carbon number affects the miscibility of alkanes and water. The temperature in the initial, dynamic, and complete miscibility stages are significantly different between different alkanes-water systems.

(3) CO_2 has a bridge function in the miscibility of alkanes and water At HTHP. Its presence significantly reduces the temperatures required for the initial, dynamic, and complete miscibility of alkanes and water.

Acknowledgements *Prof. Yong CHEN at China University of Petroleum and Prof. Xiaolin WANG at Nanjing University are thanked for their assistance in construction and improvement of high temperature quartz capillary experimental equipment. Prof. Shen WANG at China University of Petroleum is thanked for his assistance on molecular dynamics simulations. We sincerely thank the two anonymous reviewers for their significant advices and constructive comments. This work was supported by the National Natural Science Foundation of China (Grant Nos. 42222208, 41821002), the Special Fund for Taishan Scholar Project (Grant No. tsqn201909061), the Fundamental Research Funds for the Central Universities (Grant No. 20CX06067A), and Marine S&T Fund of Shandong Province for Pilot National Laboratory for Marine Science and Technology (Qingdao) (Grant No.2021QNLM020001).*

References

Bakker R J. 2012. Thermodynamic properties and applications of modified van-der-Waals equations of state. In: Morales-Rodriguez R, ed. Thermodynamics-Fundamentals and its Application in Science. New York: Cambridge University Press. 163–190

Balitsky V S, Penteley S V, Balitskaya L V, Novikova M A, Bublikova T M. 2011a. Visual *in-situ* monitoring of the behavior and phase states of water-hydrocarbon inclusions at high temperatures and pressures. Petrology, 19: 653–674

Balitsky V S, Pironon J, Penteley S V, Novikova M A, Balitskaya L V. 2011b. Phase states of water-hydrocarbon fluid systems at elevated and high temperatures and pressures: Evidence from experimental data. Dokl Earth Sc, 437: 383–386

Cao Y, Yuan G, Wang Y, Zan N, Jin Z, Liu K, Xi K, Wei Y, Sun P. 2022a. Successive formation of secondary pores via feldspar dissolution in deeply buried feldspar-rich clastic reservoirs in typical petroliferous basins and its petroleum geological significance. Sci China Earth Sci, 65: 1673–1703

Cao Y, Yuan G, Yang H, Wang Y, Liu K, Zan N, Xi K, Wang J. 2022b. Current situation of oil and gas exploration and research progress of the origin of high-quality reservoirs in deep-ultra-deep clastic reservoirs of petroliferous basins (in Chinese). Acta Petrol Sin, 43: 112–140

Carpenter I L, Hehre W J. 1990. A molecular dynamics study of the hexane/water interface. J Phys Chem, 94: 531–536

Chen H, Mi L, Liu Y, Han J, Kong L. 2017. Genesis, distribution and risk belt prediction of CO_2 in deep-water area in the Pearl River Mouth Basin (in Chinese). Acta Petrol Sin, 38: 119–134

Chen Y, Ge Y, Zhou Y, Liu C, Zhou Z, Mao C. 2009. Hydrocarbon-bearing inclusions synthesized in carbonate at temperature and pressure of natural reservoir: Some important implications for the study of petroleum geology (in Chinese). Earth Sci Front, 16: 11–16

Chen Y, Ge Y, Zhou Z. 2011. Experimental study on trapping behavior of hydrocarbon-bearing immiscible inclusions in carbonate reservoirs (in Chinese). Geochimica, 40: 536–544

Chen Y, Zhou Y, Za M, Lin C, Wang Q. 2007. Method of Raman spectroscopic quantificational analysis and computation for fluid Inclusions in CH_4-H_2O system (in Chinese). Geol Rev, 53: 814–823

Chi G, Diamond L W, Lu H, Lai J Q, Chu H X. 2021. Common problems and pitfalls in fluid inclusion study: A review and discussion. Minerals, 11: 7

Chou I M, Song Y, Burruss R C. 2008. A new method for synthesizing fluid inclusions in fused silica capillaries containing organic and inorganic material. Geochim Cosmochim Acta, 72: 5217–5231

da Rocha S R P, Johnston K P, Westacott R E, Rossky P J. 2001. Molecular structure of the water-supercritical CO_2 interface. J Phys Chem B, 105: 12092–12104

Duan Z, Lv W, Li S, Zhang W, Xie X. 2000. Computer modeling and molecular dynamics simulation of thermodynamic properties of geological fluids (in Chinese). Bull Nat Sci Found of China, 14: 112–117

Dubessy J, Moissette A, Bakker J, Frantz D, Zhang Y. 1999. High-temperature Raman spectroscopic study of H_2O-CO_2-CH_4 mixtures in synthetic fluid inclusions: First insights on molecular interactions and analytical implications. Eur J Mineral, 11: 23–32

Duan Z, Møller N, Weare J H. 2003. Equations of state for the NaCl-H_2O-CH_4 system and the NaCl-H_2O-CO_2-CH_4 system. Geochim Cosmochim Acta, 67: 671–680

Dutton S P, Loucks R G. 2010. Reprint of: Diagenetic controls on evolution of porosity and permeability in lower Tertiary Wilcox sandstones from shallow to ultradeep (200–6700 m) burial, Gulf of Mexico Basin, U.S. A. Mar Pet Geol, 27: 1775–1787

Guo H, Chen Y, Hu Q, Lu W, Ou W, Geng L. 2014. Quantitative Raman spectroscopic investigation of geo-fluids high-pressure phase equilibria: Part I. Accurate calibration and determination of CO_2 solubility in water from 273.15 to 573.15 K and from 10 to 120 MPa. Fluid Phase Equilib, 382: 70–79

Headen T F, Boek E S. 2011. Potential of mean force calculation from molecular dynamics simulation of asphaltene molecules on a calcite surface. Energy Fuels, 25: 499–502

Helgeson H C, Knox A M, Owens C E, Shock E L. 1993. Petroleum, oil field waters, and authigenic mineral assemblages Are they in metastable equilibrium in hydrocarbon reservoirs. Geochim Cosmochim Acta, 57: 3295–3339

Jia C, Pang X. 2015. Research processes and main development directions of deep hydrocarbon geological theories (in Chinese). Acta Petrol Sin, 36: 1457–1469

Jin Z, Yuan G, Cao Y, Liu K, Wang Y, Sun J, Hao X, Zhou L, Wei Y, Wu S. 2022. Interactions between hydrocarbon-bearing fluids and calcite in fused silica capillary capsules and geological implications for deeply-buried hydrocarbon reservoirs. Sci China Earth Sci, 65: 299–316

Kunieda M, Nakaoka K, Liang Y, Miranda C R, Ueda A, Takahashi S, Okabe H, Matsuoka T. 2010. Self-accumulation of aromatics at the oil-water interface through weak hydrogen bonding. J Am Chem Soc, 132: 18281–18286

de Lara L S, Michelon M F, Miranda C R. 2012. Molecular dynamics studies of fluid/oil interfaces for improved oil recovery processes. J Phys Chem B, 116: 14667–14676

Lewan M D. 1997. Experiments on the role of water in petroleum formation. Geochim Cosmochim Acta, 61: 3691–3723

Li B, Ye J, Li Z, Ji Y, Liu W. 2016. Phase interaction of CO_2-Oil-Water system and its effect on interfacial tension at high temperature and high pressure (in Chinese). Acta Petrol Sin, 37: 1265–1272, 1301

Li M, Shan W, Liu X, Shang G. 2006. Laboratory study on miscible oil displacement mechanism of supercritical carbon dioxide (in Chinese). Acta Petrol Sin, 27: 80–83

Li X, Ross D A, Trusler J P M, Maitland G C, Boek E S. 2013. Molecular dynamics simulations of CO_2 and brine interfacial tension at high temperatures and pressures. J Phys Chem B, 117: 5647–5652

Li Y, Xue Z, Cheng Z, Jiang H, Wang R. 2020. Progress and development directions of deep oil and gas exploration and development in China (in Chinese). China Petroleum Exploration, 25: 45–57

Li Z. 2016. Research frontiers of fluid-rock interaction and oil-gas formation in deep-buried basins (in Chinese). Bull Mineral Petrol Geochem, 35: 807–816

Liu Q. 2022. Hydrocarbon Accumulation Mechanism Under the Impact of Deep Fluids (in Chinese). Beijing: Science Press. 345

Liu Q, Zhu D, Meng Q, Liu J, Wu X, Zhou B, Fu Q, Jin Z. 2019. The scientific connotation of oil and gas formations under deep fluids and organic-inorganic interaction. Sci China Earth Sci, 62: 507–528

Liu Q, Zhu D, Jin Z, Meng Q, Wu X, Yu H. 2017. Effects of deep CO_2 on petroleum and thermal alteration: The case of the Huangqiao oil and gas field. Chem Geol, 469: 214–229

Lu L, Berkowitz M L. 2004. Molecular dynamics simulation of a reverse micelle self assembly in supercritical CO_2. J Am Chem Soc, 126: 10254–10255

Ma Y, Li M, Cai X, Xu X, Hu D, Qu S, Li G, He G, Xiao X, Zeng Y, Rao Y. 2020. Mechanisms and exploitation of deep marine petroleum accumulations in China: Advances, technological bottlenecks and basic scientific problems (in Chinese). Oil Gas Geol, 41: 655–672, 683

Ni P, Ding J, Chou I M, Dubessy J. 2011. A new synthetic “fluid inclusion”: The technique of optical fused silica capillary (in Chinese). Earth Sci Front, 18: 132–139

Ou W, Geng L, Lu W, Guo H, Qu K, Mao P. 2015. Quantitative Raman spectroscopic investigation of geo-fluids high-pressure phase equilibria: Part II. Accurate determination of CH_4 solubility in water from 273 to 603 K and from 5 to 140 MPa and refining the parameters of the thermodynamic model. Fluid Phase Equilib, 391: 18–30

Pang X Q, Jia C Z, Zhang K, Li M, Wang Y, Peng J, Li B, Chen J. 2020. The dead line for oil and gas and implication for fossil resource prediction. Earth Syst Sci Data, 12: 577–590

Peng D Y, Robinson D B. 1976. Two and three phase equilibrium calculations for systems containing water. Can J Chem Eng, 54: 595–599

Peng P, Jia C. 2021. Evolution of deep source rock and resource potential of primary light oil and condensate (in Chinese). Acta Petrol Sin, 42: 1543–1555

Pironon J, Grimmer J O W, Teinturier S, Guillaume D, Dubessy J. 2003. Dissolved methane in water: temperature effect on Ramanquantification in fluid inclusions. J Geochem Explor, 78-79: 111–115

Pruteanu C G, Ackland G J, Poon W C K, Loveday J S. 2017. When immiscible becomes miscible—Methane in water at high pressures. Sci Adv, 3: 1–5

Ramboz C, Pichavant M, Weisbrod A. 1982. Fluid immiscibility in natural processes: Use and misuse of fluid inclusion data. Chem Geol, 37: 29–48

Seewald J S. 2003. Organic-inorganic interactions in petroleum-producing sedimentary basins. Nature, 426: 327–333

Smith J T, Ehrenberg S N. 1989. Correlation of carbon dioxide abundance with temperature in clastic hydrocarbon reservoirs: Relationship to inorganic chemical equilibrium. Mar Pet Geol, 6: 129–135

Sun H, Ren P, Fried J R. 1998. The COMPASS force field: Parameterization and validation for phosphazenes. Comput Theor Polym Sci, 8: 229–246

Wan Y, Bourdet J, Hu W, Kang X, Heath C, Qiu Y, Gao W, Wang X. 2021. Experimental investigations on the thermochemical oxidation of n-alkane and alcohol compounds by MnO_2 and Fe_2O_3 at temperatures up to 325°C. Chem Geol, 559: 119982

Wang J. 2010. Self-diffusion and structure of pure alkanes and infinitely dilute solutions of alkanes in supercritical carbon dioxide: A molecular dynamics simulation study (in Chinese). Dissertation for Master’s Degree. Guangzhou: Sun Yat-sen University. 1–106

Wang L. 2014. Molecular simulation of oil detachment and erosion mechanism by supercritical carbon dioxide (in Chinese). Dissertation for Master’s Degree. Qingdao: China University of Petroleum (East China). 1–74

Wang X, Wan Y, Hu W, You D, Cao J, Zhu D, Li Z. 2017. Experimental studies on the interactions between dolomite and SiO_2-rich Fluids: Implications for the formation of carbonate reservoirs (in Chinese). Geol Rev, 63: 1639–1652

Wang X Y, Veld P J, Lu Y, Freeman B D, Sanchez I C. 2005. A molecular simulation study of cavity size distributions and diffusion in para and meta isomers. Polymer, 46: 9155–9161

Wang X, Chou I M, Hu W, Burrussc R C, Sun Q, Song Y C. 2011. Raman spectroscopic measurements of CO_2 density: Experimental calibration with high-pressure optical cell (HPOC) and fused silica capillary capsule (FSCC) with application to fluid inclusion observations. Geochim Cosmochim Acta, 75: 4080–4093

Wang X, Qiu Y, Chou I M, Zhang R, Li G, Zhong R. 2020. Effects of pH and salinity on the hydrothermal transport of tungsten: Insights from *in situ* Raman spectroscopic characterization of K_2WO_4-NaCl-HCl-CO_2 solutions at temperatures up to 400°C. Geofluids, 2020: 1–12

Xu X C, Chou I M. 2017. Raman spectroscopic study of cracking and hydrolysis of propane in fused silica capillary capsules between 300 and 400°C. J Raman Spectrosc, 48: 1420–1425

Yan L, Zhu S. 2013. Theory and Practice of Molecular Dynamics Simulation (in Chinese). Beijing: Science Press. 256

Yang D, Tontiwachwuthikul P, Gu Y. 2005. Interfacial tensions of the crude oil+reservoir brine+CO_2 systems at pressures up to 31 MPa and temperatures of 27°C and 58°C. J Chem Eng Data, 50: 1242–1249

Yang J, Ren Y, Tian A, Sun H. 2010. COMPASS force field for 14 inorganic molecules, He, Ne, Ar, Kr, Xe, H_2, O_2, N_2, NO, CO, CO_2, NO_2, CS_2, and SO_2, in liquid phases. J Phys Chem B, 104: 4951–4957

Yang P, Liu K, Li Z, Mcinnes B I A, Liu J. 2022. Evolution of Ordovician YJ1X ultra-deep oil reservoir in the Yuecan oilfield, Tarim Basin, NW China. Pet Explor Dev, 49: 300–312

Yang Z, Li M, Peng B, Lin M, Dong Z. 2012. Dispersion property of CO_2 in oil. 1. volume expansion of CO_2+alkane at near critical and supercritical condition of CO_2. J Chem Eng Data, 57: 882–889

Yuan G, Cao Y, Zan N, Schulz H M, Gluyas J, Hao F, Jin Q, Liu K, Wang Y, Chen Z, Jia Z. 2019. Coupled mineral alteration and oil degradation in thermal oil-water-feldspar systems and implications for organic-inorganic interactions in hydrocarbon reservoirs. Geochim Cosmochim Acta, 248: 61–87

Yuan G H, Jin Z H, Cao Y C, Liu K Y, Gluyas J, Wang Y Z, Xi K L. 2022. Evolution of $n\mathrm{C}_{16}\mathrm{H}_{34}$-water-mineral systems in thermal capsules and geological implications for deeply-buried hydrocarbon reservoirs. Geosci Front, 13: 101322

Yuet P K, Blankschtein D. 2010. Molecular dynamics simulation study of water surfaces: Comparison of flexible water models. J Phys Chem B, 114: 13786–13795

Zhang J, Fang T, Wang Y, Wang L, Shen Y, Liu B. 2015. Molecular dynamics simulation of dissolution of n-alkanes droplets in supercritical carbon dioxide (in Chinese). J China Univ Petrol, 39: 124–129

Zhang J, Pan Z, Liu K, Burke N. 2013. Molecular simulation of CO_2 solubility and its effect on octane swelling. Energy Fuels, 27: 2741–2747

Zhang Y, Tang M, Li Y, Lu L, Lu X, Zhu D, He Y, Peng Y, Huang F, Wang W. 2022. Discovery and geological significance of methane-rich fluid inclusions of Chaihulanzi gold deposit in the northern of the North China Craton (in Chinese). Acta Geol Sin, 96: 1321–1339

Zhang Z, Duan Z. 2005. Prediction of the PVT properties of water over wide range of temperatures and pressures from molecular dynamics simulation. Phys Earth Planet Inter, 149: 335–354

Zhao L B, Zhang T H, Yang X J, Guo X B, Rao H W. 2018. Gas-water distribution characteristics and formation mechanics in deep tight sandstone gas reservoirs of Keshen block, Kuqa Depression, Tarim Basin (in Chinese). Nat Gas Geosci, 29: 500–509

Zhao L, Lin S, Mendenhall J D, Yuet P K, Blankschtein D. 2011. Molecular dynamics investigation of the various atomic force contributions to the interfacial tension at the supercritical CO_2-water interface. J Phys Chem B, 115: 6076–6087

Zhong J, Wang X, Du J, Wang L, Yan Y, Zhang J. 2013. Combined molecular dynamics and quantum mechanics study of oil droplet adsorption on different self-assembly monolayers in aqueous solution. J Phys Chem C, 117: 12510–12519

Zhu D, Meng Q, Liu Q, Zhou B, Jin Z, Hu W. 2018. Natural enhancement and mobility of oil reservoirs by supercritical CO_2 and implication for vertical multi-trap CO_2 geological storage. J Pet Sci Eng, 161: 77–95

Zhu G, Li J, Zhang Z. 2021. Origin of deep oil and gas phase state diversity and evaluation of secondary geochemical intensity—A use study of marine oil and gas in Tarim Basin (in Chinese). Earth Sci, 2021: 1–17

Zhu G, Zhang Z, Zhou X, Li T, Han J, Sun C. 2019. The complexity, secondary geochemical process, genetic mechanism and distribution prediction of deep marine oil and gas in the Tarim Basin, China. Earth-Sci Rev, 198: 102930

(Responsible editor: Quanyou LIU)